Biomaterials 294 (2023) 122016

Contents lists available at ScienceDirect

Biomaterials

journal homepage: www.elsevier.com/locate/biomaterials

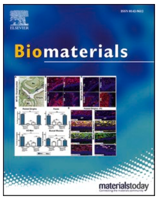

Tuning the corona-core ratio of polyplex micelles for selective oligonucleotide delivery to hepatocytes or hepatic immune cells

WanLing Foo [a], Zoltán Cseresnyés [b], Carsten Rössel [d,e], Yingfeng Teng [f], Anuradha Ramoji [g,h,i], Mingzhe Chi [f], Walter Hauswald [g], Sophie Huschke [a], Stephanie Hoeppener [b,e], Jürgen Popp [g,h,i], Felix H. Schacher [d,e], Marek Sierka [d,f], Marc Thilo Figge [b,c,d], Adrian T. Press [a,d,i,j,*], Michael Bauer [a,d,i,**]

[a] *Jena University Hospital, Department of Anesthesiology and Intensive Care Medicine, Am Klinikum 1, 07747, Jena, Germany*

[b] *Applied Systems Biology, Leibniz Institute for Natural Product Research and Infection Biology - Hans Knoell Institute, Research Group Applied Systems Biology, Beutenbergstraße 13, 07745, Jena, Germany*

[c] *Institute of Microbiology, Faculty of Biological Sciences, Friedrich-Schiller-University Jena, 07743, Jena, Germany*

[d] *Friedrich-Schiller-University, Jena Center for Soft Matter, Philosophenweg 7, 07743, Jena, Germany*

[e] *Friedrich-Schiller-University, Institute of Organic Chemistry and Macromolecular Chemistry (IOMC), Humboldtstraße 10, 07743, Jena, Germany*

[f] *Friedrich-Schiller-University, Computational Materials Science Group, Otto Schott Institute of Materials Research, Faculty of Physics and Astronomy, Löbdergraben 32, 07743, Jena, Germany*

[g] *Leibniz Institute of Photonic Technology, Member of Leibniz Health Technologies, Member of the Leibniz Centre for Photonics in Infection Research (LPI), Albert-Einstein-Straße 9, 07745, Jena, Germany*

[h] *Institute of Physical Chemistry (IPC) and Abbe Center of Photonics (ACP), Friedrich-Schiller-University, Member of the Leibniz Centre for Photonics in Infection Research (LPI), Helmholtzweg 4, 07743, Jena, Germany*

[i] *Jena University Hospital, Center for Sepsis Control and Care, Friedrich-Schiller-University, Am Klinikum 1, 07747, Jena, Germany*

[j] *Friedrich-Schiller-University, Faculty of Medicine, Kastanienstraße. 1, 07747, Jena, Germany*

ARTICLE INFO

Keywords:
PEG density
Hepatocytes
Kupffer cells
Mononuclear phagocyte system
siRNA delivery
Pharmacokinetics

ABSTRACT

Targeted delivery of oligonucleotides or small molecular drugs to hepatocytes, the liver's parenchymal cells, is challenging without targeting moiety due to the highly efficient mononuclear phagocyte system (MPS) of the liver. The MPS comprises Kupffer cells and specialized sinusoidal endothelial cells, efficiently clearing nanocarriers regardless of their size and surface properties. Physiologically, this non-parenchymal shield protects hepatocytes; however, these local barriers must be overcome for drug delivery. Nanocarrier structural properties strongly influence tissue penetration, *in vivo* pharmacokinetics, and biodistribution profile. Here we demonstrate the *in vivo* biodistribution of polyplex micelles formed by polyion complexation of short interfering (si)RNA with modified poly(ethylene glycol)-*block*-poly(allyl glycidyl ether) (PEG-*b*-PAGE) diblock copolymer that carries amino moieties in the side chain. The ratio between PEG corona and siRNA complexed PAGE core of polyplex micelles was chemically varied by altering the degree of polymerization of PAGE. Applying Raman-spectroscopy and dynamic *in silico* modeling on the polyplex micelles, we determined the corona-core ratio (CCR) and visualized the possible micellar structure with varying CCR. The results for this model system reveal that polyplex micelles with higher CCR, *i.e.,* better PEG coverage, exclusively accumulate and thus allow passive cell-type-specific targeting towards hepatocytes, overcoming the macrophage-rich reticuloendothelial barrier of the liver.

1. Introduction

Liver disease-related deaths have risen substantially between 2000 and 2020, accounting for more than 3.5% of all global deaths [1]. With approximately 800 million cases per year worldwide, liver diseases have become a significant burden on the global healthcare system [2,3]. Within the 2 million death cases per year, half are accompanied by hepatocellular carcinoma (HCC), viral hepatitis (mainly HBV), and

---

* Corresponding author. Jena University Hospital, Department of Anesthesiology and Intensive Care Medicine, Am Klinikum 1, 07747, Jena, Germany.

** Corresponding author. Jena University Hospital, Department of Anesthesiology and Intensive Care Medicine, Am Klinikum 1, 07747, Jena, Germany.

E-mail addresses: adrian.press@med.uni-jena.de (A.T. Press), michael.bauer@med.uni-jena.de (M. Bauer).

https://doi.org/10.1016/j.biomaterials.2023.122016
Received 2 August 2022; Received in revised form 6 January 2023; Accepted 14 January 2023

(other) complications of cirrhosis [4]. The therapeutic approaches and drug delivery target site vary depending on the liver disease. For instance, hepatocytes, the liver parenchymal cells, are the primary cellular target to treat HBV or inborn errors of metabolism [5,6]. However, non-parenchymal cells, most notably hepatic stellate cells (HSC), are considered the leading target site for a chronic liver disease characterized by accumulation of extracellular matrix and fibrosis [7].

Regarding the latter, RNA interference (RNAi) therapy has been developing recently as a new class of therapeutics to interfere with expressing disease-related genes in liver parenchymal and non-parenchymal cells [8–11]. RNAi therapeutics, becoming a high potential treatment for liver diseases, arrived at a new era when the first FDA-approved siRNA drug Patisiran by Alnylam Pharmaceutical, was launched in 2018 [12]. Patisiran represents a lipid nanoparticle loaded with siRNA explicitly targeting hepatocytes for the treatment of hereditary transthyretin-mediated (ATTR) amyloidosis [13]. Conventional lipid nanoparticles, the most intensively characterized and used drug/-gene delivery system in the past few decades, require multiple-step and precise synthesis procedures. Producing lipid drug/gene carriers often involves time-consuming processes, including chemical deprotection, solvent exchange, catalyst removal, and purification [14]. Furthermore, evidence suggests that lipid-formulated siRNA carriers might induce unwanted innate immune responses, *e.g.,* reflected in cytokine release [15,16]. In recent years, polymeric carrier systems with PEGylation have been shown to reduce the adsorption of opsonin proteins, which could increase their stealthiness and retention in the bloodstream [17,18]. Fisher et al. and Walkey et al. further discovered that PEGylating quantum dots and increasing polyethylene glycol (PEG) density of gold nanoparticles prevent the uptake by Kupffer cells and macrophages [19,20]. Mosquiera et al. further strengthened the theory of PEGylation on reducing nanocapsules' elimination from the body and emphasized the importance of PEGylation's degree in affecting the nanoparticles' biodistribution [17]. Block copolymers with PEG modification on the surface, PEG-*b*-catiomers, have been extensively reported in well-protecting siRNA and could effectively facilitate the delivery path to exhibit therapeutic effects *in vivo* [21–26]. The stability and biophysical properties of siRNA polyplexes formed by PEG-PEI enhanced significantly with higher molecular weight (M_w) of PEG. PEI(25 k)-*g*-PEG(20 k) and PEI(25 k)-*g*-PEG(5 k) showed superior ability in protecting siRNA against RNase and improved gene silencing efficacy in comparison with PEI(25 k)-g-PEG(2 k) [23]. Instead of varying the degree of PEGylation, changing the length of the grafting polymer on PEG while maintaining the same M_w of PEG could also affect the PEG crowdedness, the physicochemical properties, and the transfection efficiency of the polyplex. Several studies published on plasmid DNA (pDNA) polyplexes with PEG-polylysine (PLys) indicated that different degrees of polymerization of PLys dramatically influence the size and shape of pDNA polyplexes. The difference in the PEG crowdedness and physicochemical properties of these pDNA polyplexes lead to a variation in their distribution and blood retention profile [27–30]. Shorter PLys increased the PEG crowdedness of polyplexes resulting in a larger diameter of more than 200 nm. Furthermore, they deteriorated their cellular uptake capability and transfection efficiency [18,28,30]. Despite the large nucleic acid oligomer, the research on how the length of the catiomers on PEG-*b*-catiomers affects the physicochemical and biological properties of small oligonucleotide siRNA polyplexes is limited.

The liver, comprising most of the mononuclear phagocyte system (MPS), sequesters and excretes 30%–99% of all nanoparticles after systemic administration [31]. Thus, targeted nanoformulated drugs to reach hepatocytes in the liver are frequently sequestered by the local MPS (Kupffer cells, KCs, liver sinusoidal endothelial cells, LSECs). Thereby they would lose their therapeutic effect. Therefore, cell-type-specific targeting of hepatocytes remains challenging for polymer-based nucleic acid delivery. Structural properties of nanocarriers contribute significantly to their distribution between different cell types of the liver. Particularly, nanocarriers with sub-100 nm diameter have been proven helpful for penetrating thick fibrotic layers, and several labs have investigated their accumulation in target cells [30,32]

siRNA encapsulated nanogels with a smaller average diameter (40 nm) have also shown superior gene silencing efficacy compared to their larger counterparts (100 nm) [33]. However, the effect of the hydrodynamic size or the molecular weight of a present PEG corona directing the distribution of the siRNA nanocarriers toward hepatocytes and Kupffer cells had not been wholly conceptualized [34]. Covalently conjugated targeting moieties on nanoparticles and micelles are established methods to increase their accumulation in hepatocytes [35]. Despite a medical need for improved hepatocellular drug and nucleic acid delivery, there are few investigations on the passive targeting of hepatocytes at a cellular level via tuning and optimizing physicochemical properties.

Our previous work demonstrated that the charge, structural properties, and interaction between cargo and carrier during encapsulation drastically affect micelle formation, cargo distribution, and drug release [36,37]. Here, we established a series of siRNA polyplex micelles formed with a simple diblock copolymer system with PEG as a hydrophilic block and PAGE as a segment for the subsequent introduction of cationic binding sites. The PAGE segment with cationic charges allows polyion complexation with anionically charged siRNA, forming the core of the polyplex micelles with PEG as a corona. Furthermore, PEG with constant molecular weight combined with varying degrees of polymerization for PAGE allows fine-tuning the corona-core ratio (CCR) on the resulting siRNA polyplex micelles. Here, we investigated different combinations of PEG and PAGE with their resulting CCR as they affect the encapsulation and delivery of oligonucleotides to hepatocytes or immune cells.

2. Results and discussion

2.1. Polyion complexation of siRNA into polyplex micelles with different corona-core ratios

The manuscript utilizes the PAGE chain numbers (15, 29, 60, and 76) to discriminate the polyplex micelles. Each polyplex micelle is further associated with a theoretical and measured "corona-core ratio" (CCR) dependent on the PAGE-core and PEG-corona size, summarized in Table 1. The ratio of the number average molar weight (M_n) from the PEG and PAGE block determines the CCRs of PEG-*b*-$PAGE_{NH2}$ diblock copolymers-based polyplex micelles (EN15, EN29, EN60, and EN76) (Table 1 and Fig. 1a). The CCR is associated with the PEG corona density of the polyplex micelles and, therefore, may determine the pharmacokinetics of the polyplex micelles. Here, we investigated siRNA polyplex micelles EN15, EN29 EN60, and EN76 with a broad range of CCRs. The micelles are obtained by polyion complexation of blunt-ended oligonucleotides (siRNA) and hydrophilic PEG-*b*-$PAGE_{NH2}$ diblock copolymers. Different degrees of polymerization of the PAGE segment and a fixed block length of PEG (DP = 42 and $M_w = 2000\ g\ mol^{-1}$) resulted in different CCRs. The diblock copolymer precursors were synthesized by anionic ring-opening polymerization of allyl glycidyl ether (AGE) with deprotonated poly(ethylene glycol) monomethyl ether (PEG) as macroinitiator (Scheme 1). The length of the PAGE segment in the four polymers is 15, 29, 60, and 76 repeating units and modified with cysteamine through thiol-ene click reaction to introduce amino groups (-NH_2) for later complexation with siRNA (Scheme 1). All synthesized polymers were characterized by size exclusion chromatography (SEC) and ^1H NMR spectroscopy (Supplementary Information I Figure SI 1). The degree of functionalization with primary amino groups was determined by ^1H NMR spectroscopy using the residual polymer pendant allyl signals of PAGE at 3.9–4.1, 5.0–5.4, and 5.7–6.0 ppm (Figure SI 1d). All functionalized neat diblock copolymers PEG-*b*-$PAGE_{NH2}$, denoted as EN15_poly, EN29_poly, EN60_poly, and EN76_poly, carry cationic charged amine groups present in the side chain of the PAGE segment

Table 1
Physicochemical properties of siRNA polyplex micelles, formed by 22 bp blunt-ended siRNA and PEG:PAGE with different lengths of PAGE.

Polyplex micelles	M_n of PEG[a] (g mol^{-1})	Dp of PAGE[b]	M_n of PAGE[a] (g mol^{-1})	CCR (M_n ratio of PEG:PAGE)	Peak area ratio[c] (860 cm^{-1}/650 cm^{-1}) (PEG:PAGE)	Size[d] d_h (nm)	PDI	Zeta Potential (mV)	Averaged diameter[e] (nm)
EN15	1865	15	2808	0.66	0.66	71	0.25	24	66
EN29	1865	29	5556	0.34	0.24	60	0.35	22	58
EN60	1865	60	11485	0.16	0.19	104	0.23	29	69
EN76	1865	76	14579	0.13	0.18	101	0.23	30	94

[a] M_n was calculated using SEC.
[b] ^{1}H NMR determined the degree of polymerization of PAGE.
[c] The peak area ratio measured by Raman Spectroscopy represents the CCR of different polyplex micelles.
[d] DLS determined the hydrodynamic diameter.
[e] The average diameters of polyplex micelles measured from TEM images, n > 50 particles.

(Fig. 1a). This series of PEG-*b*-PAGE$_{NH2}$ with a constant molecular weight of the PEG block and different PAGE segments allows altering the CCR of the polyplex micelles after complexation with oligonucleotides (Fig. 1a). The ratio of moles of the amine groups on the cationic polymers to anionic phosphate groups in the RNA backbone of the oligonucleotide determines the nitrogen to phosphate (N/P) ratio. Cationic diblock copolymers are complexed with anionically charged siRNA at an N/P ratio of 5, giving rise to the formation of micelles EN15, EN29, EN60, and EN76. At the same N/P ratio, the mass of neat polymers required to complex with an equal amount of siRNA differs due to varying amounts of cationic charges from the PAGE block. Thus, in EN15, with the shorter PAGE segment, more PEG-*b*-PAGE$_{NH2}$ is required to complex siRNA than EN60 or EN76 (Fig. 1b).

Gel retardation assay (GRA) and ethidium bromide (EtBr) assay confirmed complete complexation of the siRNA at an N/P ratio of 5 (Supplementary Information I Figure SI 2) and stability (Supplementary Information I Figure SI 7). All polyplex micelles and a naked siRNA sample were kept at 21 °C for 7 days simulating shelf aging. We then incubated the aged samples for 3 h at 37 °C, rocking in the presence of 10% human serum or 10% Krebs-Henseleit Buffer (KHB). KHB was chosen as the reference buffer since it closely resembles the ion composition of human blood but does not contain RNases and other proteins that may destabilize the micelles or could degrade the siRNA cargo. The naked siRNA remained intact after 7 days at 21 °C and 37 °C incubation with KHB, but the addition of 10% serum resulted in its complete degradation (Supplementary Information I Figure SI 7). On the other hand, all micelles remained intact and protected the siRNA successfully from degradation by serum proteins (Supplementary Information I Figure SI 7a). To demonstrate that the siRNA in the micelles are still intact after serum incubation, we heated an aliquot of each sample to inactive serum proteins and induced a siRNA release by acidifying the solution directly before loading it on the GRA (Supplementary Information I Figure SI 7b). Notably, a distinct RNA signal appeared for all samples where the micelles had protected the siRNA during the 3 h incubation with KHB or serum. Furthermore, the free siRNA was again completely degraded by serum addition, indicating the stability of the micelles but not free siRNA in the presence of serum.

Additionally, we heated a subset of each sample to inactive serum proteins after the 3 h incubation and induced the siRNA release by acidifying the solution (Supplementary Information I Figure SI 7 B). Notably, a clear RNA signal appeared for all samples where the micelles had protected the siRNA during the 3 h incubation with KHB or serum. Furthermore, the free siRNA was again completely degraded by serum addition, indicating the stability of the micelles in the presence of serum even after aging for 7 days at 21 °C. The size and zeta potential of the polyplex micelles were characterized by dynamic light scattering. The polyplex micelles were somewhat similar in size ($d_h = 60$–101 nm) and characterized by a low homogenous polydispersity index (PDI) ranging from 0.23 to 0.35 (Table 1). In addition, all polyplex micelles possess cationic zeta potential in the range of 22–30 mV. The TEM images confirmed the spherical shape of all the polyplex micelles (Fig. 1c). The diameters of polyplex micelles measured from TEM are presented in the histogram (Fig. 1d, Table 1). The size discrepancy between DLS and TEM may result from the collapsed polymer structures due to a loss of solvent during TEM preparation. At the same time, DLS provides the hydrodynamic size of polyplex micelles in an aqueous buffer. Wilson et al. reported a qualitative and quantitative study on the size difference of PEG-polystyrene measured by DLS and TEM. A shrinkage in the TEM-measured compared to the DLS diameter was reported [38]. Besides, the PEG corona on the polyplex micelles may not be visualized in TEM due to the higher contrast of Cy3 labeled siRNA in the core [28,39]. Hence, the diameters measured using TEM show only the hydrophobic core of the polyplex micelles, which is smaller than the hydrodynamic radius extracted from DLS data.

To investigate the relationship between polyplex micelles with different CCRs, we performed Raman spectroscopy on each micelle prepared using 22 base pairs (bp) siRNA with respective diblock copolymers or the siRNA alone. The polyplex micelles were prepared at an N/P ratio of 5 with the corresponding concentration of block copolymers. Raman spectroscopy provides information about molecular vibrations and is specific to the type and interaction of the molecules in a given environment. Thus, molecular bonds in a macromolecule highly complexed by their environment will have minor contributions to the Raman signal from the polymer side chain. Still, if the same bond in this macromolecule is free to vibrate, it will strongly contribute to the Raman signal. Utilizing the Raman peak information observed in each polyplex micelles' Raman spectra, information on the micellar conformation can be obtained and compared between different CCRs. All tested materials provided unique Raman signatures. Raman spectra were acquired from all polyplex micelles (EN15, EN29, EN60, and EN76) and their corresponding neat polymers for reference (Figure SI 2c, d). From the spectra, polyplex micelles EN15 exhibited a strong Raman signal at the 1449 cm^{-1} vibration peak, attributed to the CH_2 stretching from the PEG block (Figure SI 2c) [36]. While the spectra of EN60 and EN76 show more substantial vibration peaks at 646 cm^{-1}, the C–S stretching contributed from PAGE blocks due to the higher amount of PAGE repeating units. The vibration peaks 1449 cm^{-1} (PEG) and 646 cm^{-1} (PAGE) appear with somewhat similar intensities in EN29. Moreover, all polyplex micelles exhibit two significant peaks arising from siRNA, at 1036 cm^{-1}, the vibration contributed from ribose, and 1143 cm^{-1}, representing the phosphate group stretching (Figure SI 2c).

To further examine the systematic differences, we subjected Raman spectra of all polyplex micelles, siRNA, and corresponding neat polymers to an unsupervised principal component analysis (PCA). PCA is a powerful tool for identifying variations and spectral differences between data groups. By preprocessing the Raman spectra, non-contributing variances such as noise and background are removed. The dimensionality of the Raman data is reduced by linear transformation into a new coordinate system where the group variance information is captured onto the principal components (PC), and PC scores are calculated. The PC scores are plotted for visualization of the group differentiation. This study uses PCA to explore and highlight Raman spectral variations in the

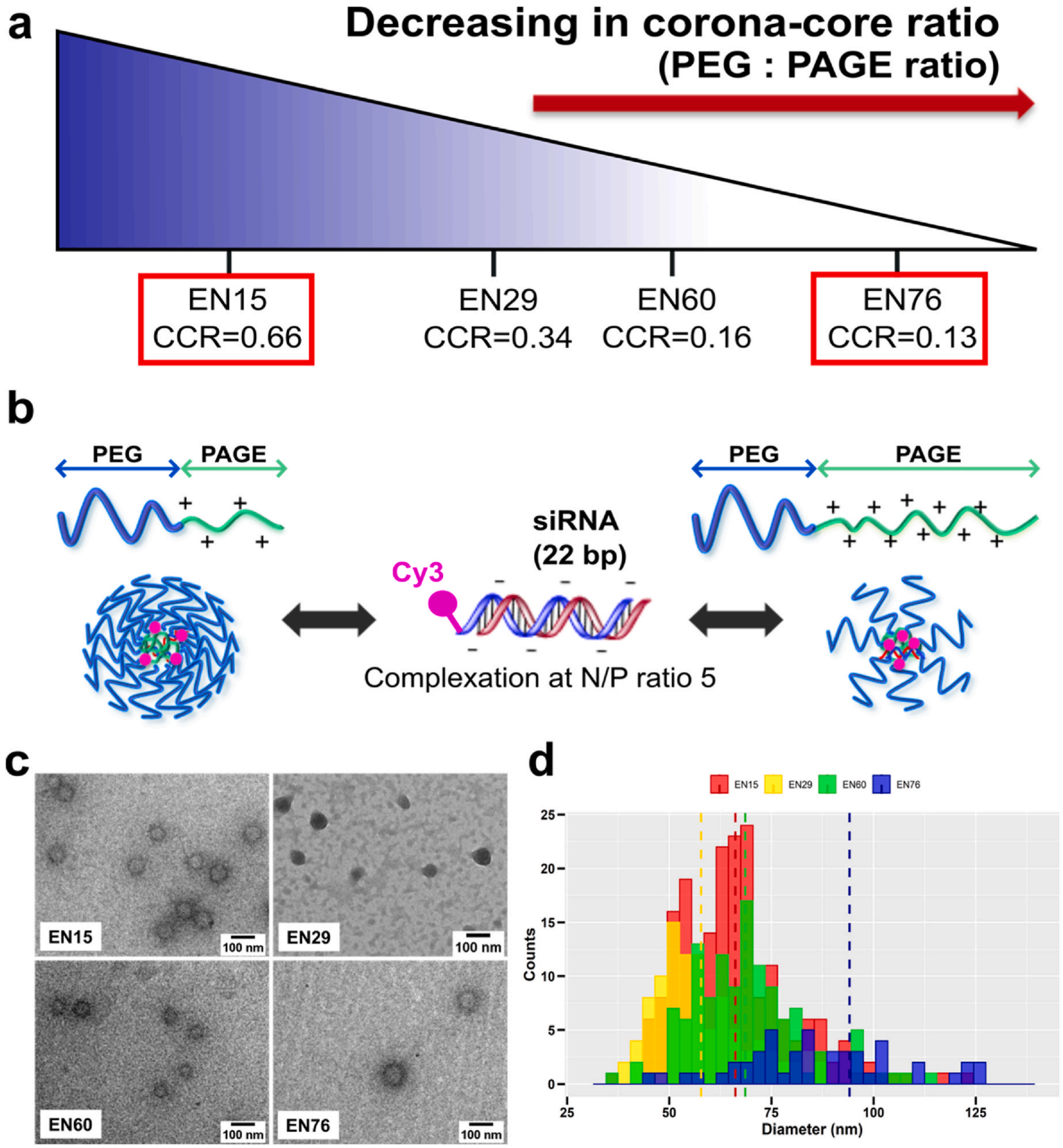

Fig. 1. Illustration graph of siRNA complexes with different block copolymers with different CCR and their morphology. (a) The illustration of the CCR for each siRNA polyplex micelles was calculated from averaged molar weight (M_n) of the PEG corona and M_n of PAGE core. The calculation is presented in Table 1. (b) Scheme of polyion complexation between siRNA and diblock copolymer. 22 base pair Cy3 labeled siRNA was complexed with EN15_poly and EN76_poly at N/P ratio 5. (c) TEM images suggest a spherical shape of all polyplex micelles. (d) Histogram of the polyplex micelles' diameters. The diameter of polyplex micelles was measured from TEM images, and at least 50 particles were measured for each type of polyplex micelles. All micelles were formed at an N/P ratio of 5.

different investigated micelles. The PC1 and PC2 differentiate the micelles and the respective PC loadings, indicating the spectral variances among the groups. For clarity, PC score plots have been displayed by highlighting only the PC scores of the neat polymer (Fig. 2g) and the PC scores of micelles (Fig. 2h), both with siRNA PC scores for comparison. While EN29, EN60, and EN76 (with a low CCR) and their neat polymers clustered similarly (positive PC2 scores), they show a clear difference between EN15 and the siRNA with positive PC2 scores (Fig. 2g and h). The PC loadings in Fig. 2i show the contribution of different Raman peaks responsible for the groups' classification in PC1 and PC2. In PC1, the significant contribution to the differentiation comes from the Raman peak at 646 cm^{-1} (C–S stretching) originating from the PAGE block, *i.e.*, the core (Fig. 2i) [36]. The PC2 differentiation is a result of the PEG-CH_2 stretching at the corona with peaks at 777 cm^{-1}, 843 cm^{-1} (EN29, EN60, EN76), and 1449 cm^{-1} (EN15) (Fig. 2i) [36,40]. Further contributions observed in PC1 and PC2 to the differentiation were assigned to the siRNA molecule (792, 995, 1327, 1569/1576 cm^{-1}, RNA vibrations) [41] as summarized in the Supplementary Information I (Table SI 3). The Raman peak area represented the signal strength. It was utilized to calculate the peak area ratio of the PEG (843 cm^{-1}) and PAGE (646 cm^{-1}), which depicted a value similar to the theoretical CCR ratio obtained from the M_n of the individual PEG and PAGE blocks for different micelles (Table 1, Figure SI 2e). The different CCRs and the Raman vibrational fingerprints of EN15, EN29, EN60, and EN76 captured in the PCA, suggest variations in the structural properties of all investigated micelles.

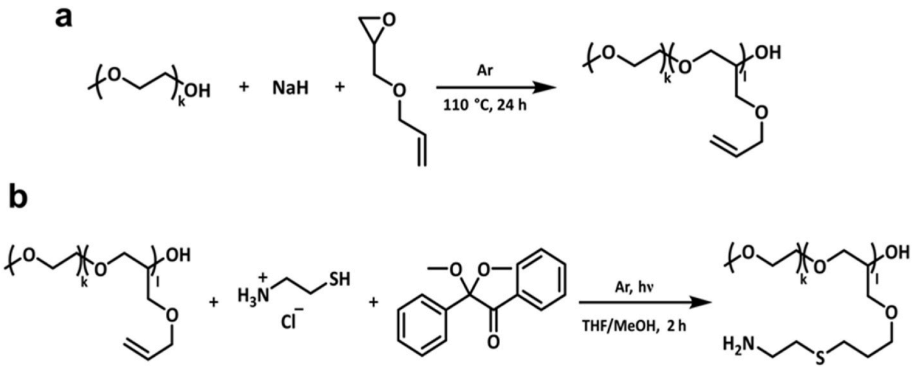

Scheme 1. Preparation of the cationic polymers as gene carriers. (a) Synthesis of PEG_{42}-*b*-PAGE with an increased PAGE block of 15, 60, and 76 repeating units by ring-opening polymerization followed by (b) a functionalization on the PAGE segment with primary amines *via* thiol-ene click reaction.

2.2. *In silico modeling of micellar architecture*

Although micellar gene delivery systems have been extensively studied using various experimental characterization techniques, detailed atomic and nanoscale information about the internal structures and complexation mechanism remains challenging [42,43]. In recent years, computer simulations by *in silico* modeling have emerged as a powerful tool for understanding the formation and structure of micelles. In particular, Dissipative Particle Dynamics (DPD) simulations have been performed and used extensively to simulate amphiphilic block copolymers at the mesoscale to gain insight into the structure and properties of various CCR micelles [44]. Using charge neutral beads, we have performed DPD simulations of siRNA encapsulation and micelle formation for EN15, EN29, EN60, and EN76 (Fig. 3). The coarse-grained models of polymer chains were built based on the experimental DP values (Table 1), and the siRNA model was built based on the TLR4 sequence (Table 2). Since simulations of actual micelles would be too computationally demanding even for DPD, we used smaller models that contained only one siRNA molecule and enough polymer material for its complete encapsulation. Nevertheless, such models are still expected to provide a qualitative picture of siRNA-polymer arrangement within these polyplex micelles [45,46]. Further details of the DPD simulations are provided in Supplementary Information II.

The results obtained for EN15 (Fig. 3a and b), EN29 (Fig. 3c and d), EN60 (Fig. 3e and f), and EN76 (Fig. 3g and h) showed different trends. In the initial stage of DPD simulations, all polyplex micelles with siRNA formed disordered distribution of beads. As the simulations progressed, EN15, EN29, and EN60 gradually formed a layered micelle, with the hydrophilic PEG beads building an outer layer and the PAGE beads accumulating around the siRNA core. After 10000 time steps, the micelle structure became stable and maintained its stability for the remaining 10000-time steps (20000-time steps for the entire DPD simulation). The cross-sectional views in Fig. 3b, 3d, and 3f demonstrate that EN15, EN29, and EN60 fully encapsulate the siRNA molecule in the core. Simulations further revealed a gradual decrease in the PEG layer's thickness from EN15, EN29 to EN60. EN76 (Fig. 3g) showed similarly disordered structures in the initial simulation stages as the other micelles. However, a disrupted PEG corona formed in the final micelle structure, with the siRNA partially exposed on the surface of the micelle (Fig. 3g and h). Simulations with charged beads were also performed for EN15 to investigate the influence of bead charge on DPD results (Supplementary Information I Figure SI 3). The structure of siRNA changed slightly, but the EN15 micelles remained stable and showed little structural change compared to DPD simulations employing charge-neutral beads. The consistent results observed for EN15 with the different simulations indicate that the short-range electrostatic interactions included implicitly in the DPD force field parameters have the most substantial influence on the structure of the micelles. The simulation results show that all the block copolymers (EN15, EN29, and EN60) form micellar polyplex structures complexing siRNA, but only EN76, not fully encapsulated siRNA.

The findings of DPD modeling were further investigated via an experiment with free-flow electrophoresis of EN15 and EN76 (Supplementary Information I Figure SI 4). The difference in the PEG corona density might alter the ability of the micelles to interact with serum proteins. To investigate this hypothesis, we performed free-flow electrophoresis [47] on the micelles incubated with Krebs-Henseleit buffer (KHB) in the presence and absence of 20% human serum. The micelles injected from a central channel of the electrophoretic bed were separated at 1250V-1500 V for 7 min in a D-Histidin buffer system at pH 6.5. Ninety-six fractions were then collected from the outlet in a well plate, and Cy3-labeled siRNA was detected through the specific Cy3 fluorescence (excitation/emission) using a plate reader (Figure SI 4a).

EN15 in KHB without serum was less affected by charged interactions, as shown by the near central outflow Cy3 peak concentration in fractions 47–52 (Figure SI 4b). However, EN76 was very sensitive to the applied electrophoretic charge, and the siRNA signal migrated to the fractions closest to the negative pole (82–90) (Figure SI 4d). In the presence of serum, EN76 electrophoresis resulted in a peak-broadening and a second peak closer to the anode than EN15 (Figure SI 4c). Those changes indicate serum protein interaction with a fraction of EN15 micelles, making the micelles more positive and sensitive to the applied electrophoretic current. In EN76, with lower CCR, the siRNA peak broadened and shifted from fractions 82–90 to 47–90. In addition, two peaks at more negative fractions are apparent (10–15 and 47–51), all indicating more vital interaction with serum proteins (Figure SI 4e).

After applying a current in the free-flow electrophoresis, the differences in the EN15 and EN76 shifts support the hypothesis that micelles interact differently with serum proteins due to CCR changes.

2.3. *In vitro characterization of micellar pharmacokinetics/pharmacodynamics*

All polyplex micelles (EN15, EN29, EN60, and EN76) are biocompatible and did not lead to a release of lactate dehydrogenase (LDH) from the cells into the supernatant (Fig. 2a). The observation from *in vivo* experiments later confirmed the biocompatibility of all polyplex micelles. Animals injected with highly concentrated polyplex micelles (30 μg siRNA per animal) showed no signs of acute discomfort. Therefore, we transferred all polyplex micelles into an *in vitro* model to investigate their ability to deliver their cargo and induce RNA interference (RNAi) by delivering a Cy3-labeled siRNA (Cy3-siRNA) cargo. The isolation and cultivation of primary liver cells are challenging and unsuitable for extensive screenings due to batch-to-batch variability that can mask the effects. Thus, the HeLa system was selected instead owing to its stability and reproducibility in screening assays. The mean fluorescence Cy3-siRNA intensity in the transfected cells quantified the uptake of the polyplex micelles in HeLa cells. Throughout 24 h, EN29, EN76, and

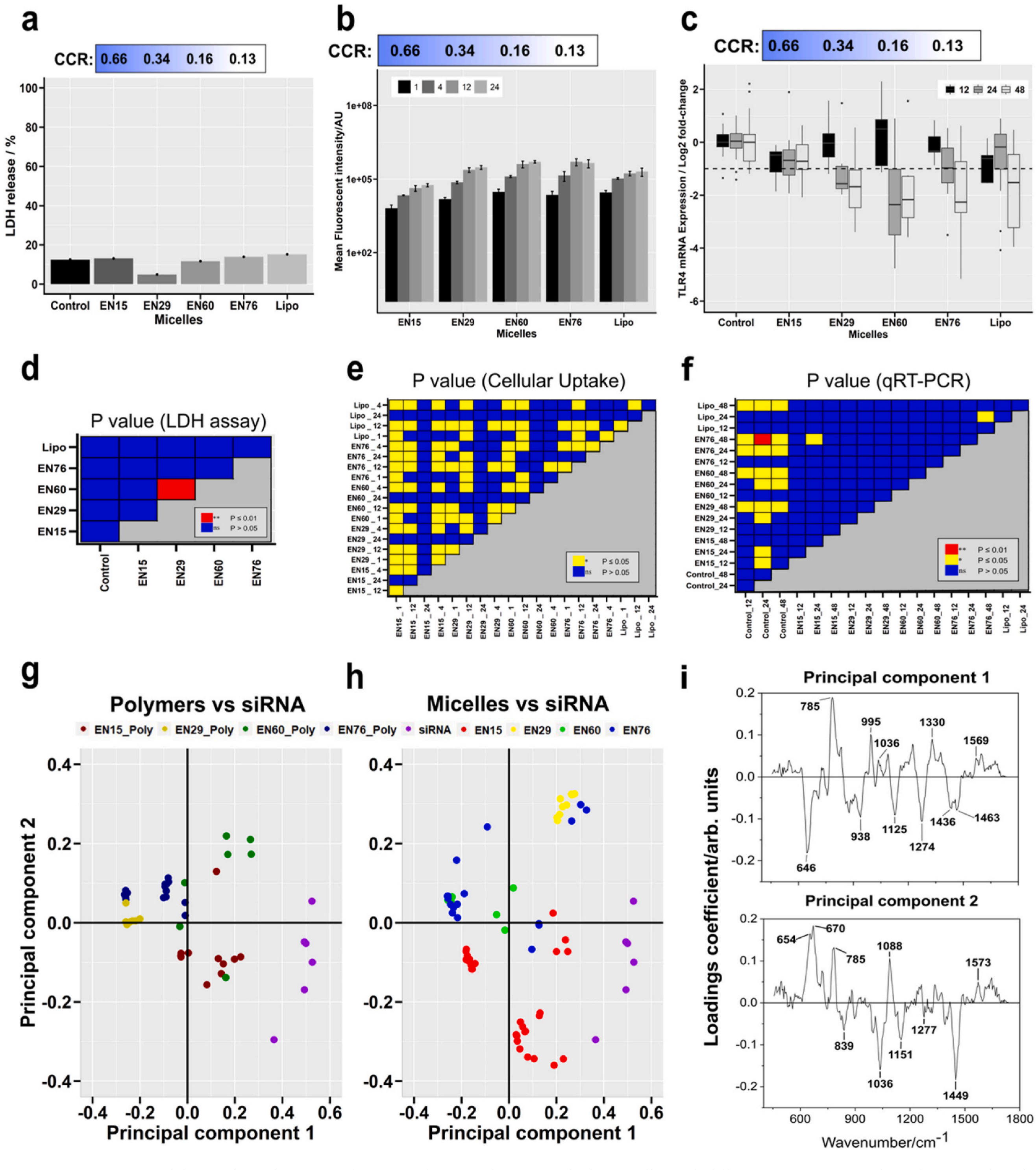

Fig. 2. *In vitro* comparison of the uptake and RNA interference performance between polyplex micelles with different CCRs (a) LDH release from transfected HeLa cells 24 h after incubation with (siTLR4) loaded micelles (n of 3 per group). (b) Cellular uptake of Cy3-siRNA complexed with different polyplex micelles or Lipo (positive control) was analyzed by flow cytometry at individual time points. (c) *TLR4* mRNA expression analysis in HeLa cells at different time points after their transfection with EN15, EN29, EN60, or EN76 loaded with a Cy3-siRNA against *TLR4* (siTLR4). The horizontal dotted line indicates a 50% knockdown of mRNA expression. In addition, Gene expression was normalized against a *TCF7L2* as a reference gene and compared to non-transfected controls. Lipofectamine RNAiMax (Lipo) served as a positive control. The quantification of *TLR4* mRNA was done in at least three replicates, and the expression changes were presented as a Tukey-box plot. (d–f) The significant test is performed using the Pairwise Wilcoxon (Rank Sum) Test with a Benjamini Hochberg p-value adjustment to correct the multiple testing. The exact significant values between each sample group are plotted in (d) LDH assay (Fig. 2a), (e) cellular uptake (Fig. 2b), (f) qRT-PCR (Fig. 2c), (g–i) Principal component analysis on Raman spectra of siRNA versus (g) different polyplex micelles or (h) only accessible diblock copolymers (EN15_poly, EN60_poly, and EN76_poly). Results are obtained from combined PCA evaluation of all polyplex micelles and diblock copolymers and are plotted into two figures for easy comparison. (i) PCA loadings coefficients PC1 and PC2 showing contributions of Raman peaks. Raman spectral data was acquired from at least three different sampling positions, and from each position, at least five spectra were acquired. The number of spectra of all groups is present in Table SI 4. An N/P ratio of 5 was used for micelles in the experiments.

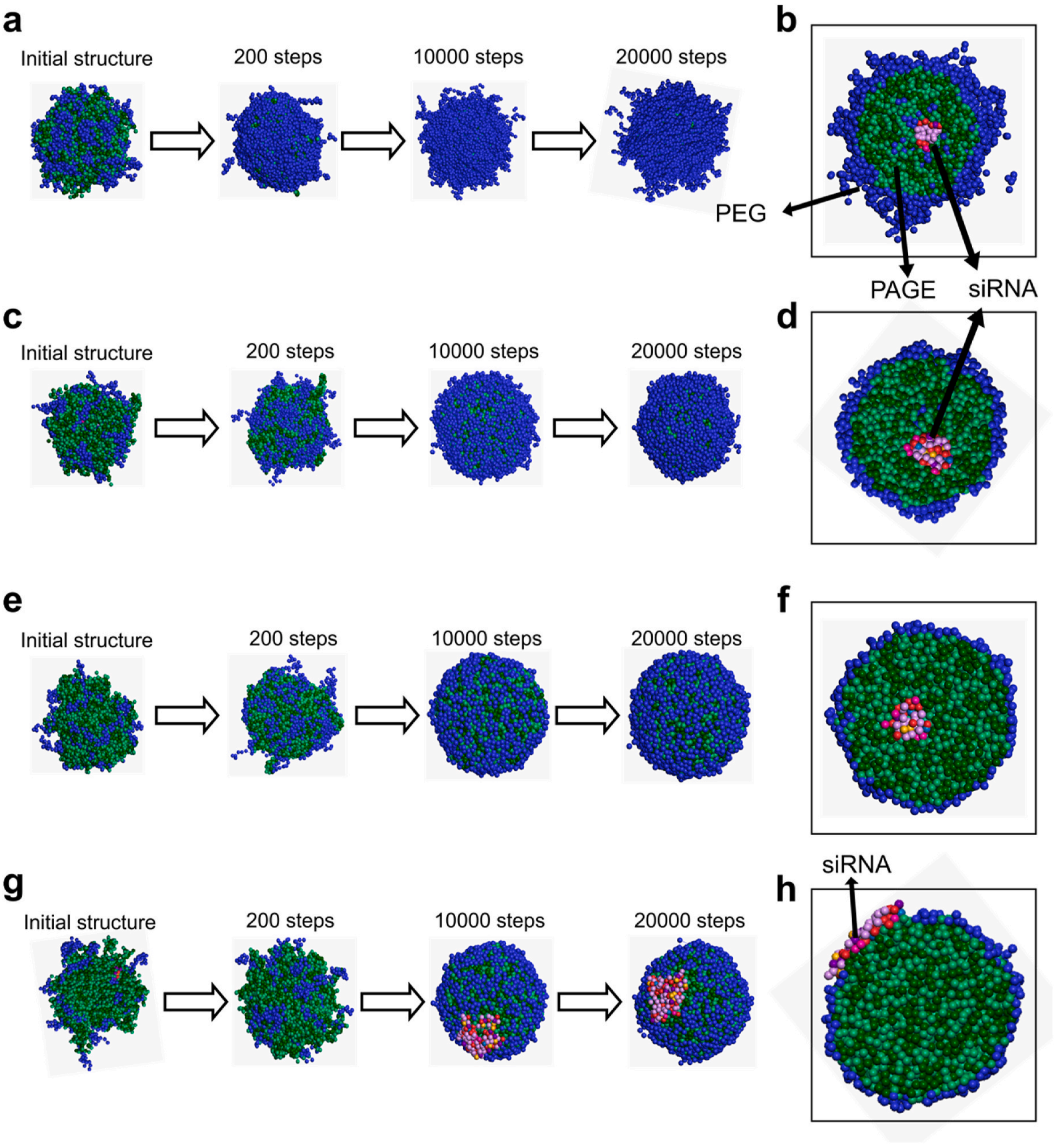

Fig. 3. Snapshots of DPD simulations showing the formation and structure of polyplex micelles complexed with siRNA (water beads are hidden for clarity): (a) EN15 and (b) cross-sectional view of the final micelle; (c) EN29 and (d) cross-sectional view of the final micelle; (e) EN60 and (f) cross-sectional view of the final micelle; (g) EN76 and (h) cross-sectional view of the final micelle.

EN60 with a lower CCR ratio, *i.e.*, thinner PEG corona, were rapidly taken up compared to EN15 with a higher CCR (Fig. 2b). However, uptake is only one of the steps in the delivery process of siRNA into the cytosol. Thus we quantified the gene silencing using Toll-Like Receptor 4 (TLR4) as a marker gene for RNAi efficacy. HeLa cells incubated with the polyplex micelles prepared with a siRNA against *TLR4* were harvested and analyzed after 12, 24, or 48 h. The mRNA expression was quantified using a one-step reverse-transcription quantitative PCR. *TLR4* expression was normalized to *TCF7L2* as a reference gene [48,49]. The knockdown is then expressed as a $\log_2$-fold change compared to untreated controls. Transfection with commercial Lipofectamine RNAiMax (Fig. 2c, Lipo) was a positive control. Even though RNAi for EN29, EN60, and EN76 was more pronounced than for EN15, which might be a result of the reduced uptake due to a better PEG-shielding, EN15 still exhibits nearly 50% knockdown of the mRNA expression (Fig. 2c).

2.4. *In vivo distribution of siRNA polyplex micelles with different CCRs*

The non-parenchymal cells, particularly LSEC and KC, constitute the most considerable fraction of the liver's MPS. Together these cells shield the parenchymal cells, *i.e.*, the hepatocytes, from foreign bodies and may trigger a local or systemic immune response. To evaluate passive hepatocyte targeting and biodistribution as a function of the polyplex micelles CCR, we performed intravital microscopy (IVM) in FVB/N mice. After 1 min of baseline image acquisition on liver tissue, polyplex micelles containing Cy3-siRNA were injected into the tail vein of the mouse, followed by 45 min time-lapse imaging. The basic liver architecture was imaged employing the contrast between hepatocyte NAD(P)H autofluorescence (blue) and the non-fluorescent vessels (black) at 405 nm illumination. EN15 with a high CCR accumulated in hepatocytes within 15 min. EN76, EN60, and EN29, with a low CCR ratio, showed a

Table 2
The Oligonucleotides are used to form polyplex micelles in all physicochemical properties characterizations, *in vitro,* and *in vivo* evaluation.

Oligonucleotide		Sequence (5′ to 3′)	Modification	Target
Toll-like receptor 4 (TLR4)	Sense (22 bp) $T_m = 54$ °C	[2OMeU]CAUAUUCAAAGAUACACCCCC	5′-O-methyl-U	*TLR4*, NM_138554.4
	• Antisense (22 bp) $T_m = 54$ °C	[2OMeG]GGGGUGUAUCUUUGAAUAUGA	5′-O-methyl- G	
Cy3-Scum	Antisense (22 bp) $T_m = 58.4$ °C	[CY3] TCAAACGTACGTTACGGGTCTT	5′-Cy3	None
Cy5-Scum	Antisense (22 bp) $T_m = 58.4$ °C	[CY5] TCAAACGTACGTTACGGGTCTT	5′-Cy5	
Scum	Sense (22 bp) $T_m = 58.4$ °C	AAGACCCGTAACGTACGTTTGA	–	
	Antisense (22 bp) $T_m = 58.4$ °C	TCAAACGTACGTTACGGGTCTT	–	

All oligonucleotides are provided by Eurofins Genomics (Ebersberg Germany); * Cy: Cyanine; 2OMe: 2′-O-Methylation.

lower accumulation in hepatocytes over the IVM duration. EN76 even depicted a slight reduction in uptake (Figs. 4a and 5a). The hepatocellular uptake was established when two features were present: an overlay of the Cy3 fluorescence with the NAD(P)H autofluorescence of hepatocytes, and the appearance of line patterns inside hepatocytes, resembling canaliculi, a network of ducts of approximately 1 μm in diameter [50] and that form the first section of the biliary system, which hepatocytes use to eliminate endo- and xenobiotics (Fig. 5a).

Circulating immune cells were identified in time-lapse images by their movement, while KC remained immobile within the imaging period (Fig. 5b). Quantification of Cy3 fluorescence intensity in the hepatocyte, immune cells/KC, and sinusoids are analyzed by an automated image analysis algorithm written in JIPipe [51] (Supporting Information III Fig. 4). Cell types can be discriminated from intravital microscopy images due to differences in NAD(P)H autofluorescence and their location within the tissue. A recent publication validated the automated image analysis approach provided by JIPipe when the microanatomical features of different liver cell types from intravital microscopy image data were used to quantify cell-type-specific uptake and distribution [52]. The hepatocellular fluorescence was quantified by segmenting the tissue through its autofluorescence (NADPH for hepatocytes), subtracting the canalicular line patterns, and analyzing Cy3 fluorescence over 30 min (Fig. 4a and b). The kinetic curves shown in Fig. 4a reveal a distinct accumulation profile of all polyplex micelles. The area under the curve (AUC) of Cy3 fluorescence intensity was calculated from each kinetic curve in a 30 min interval. The AUC, *i.e.*, the uptake in hepatocytes, was significantly reduced in EN76, EN60, and EN29 compared to EN15 (Fig. 4b). In line with this observation, the maximum Cy3 fluorescence intensity captured in hepatocytes was also lower in EN76, EN60, and EN29, with a lower CCR than in EN15 (Fig. 4c). The quantification of AUC from the kinetic curve over 30 min in KC and circulating immune cells is reported in Fig. 4d. The results show that the mean fluorescence intensity of EN60 and EN76 in circulating immune cells and KC is higher than that observed for EN15 and EN29, indicating the higher uptake of EN76 and EN60 in immune cells. The maximum fluorescence intensity measured in circulating immune cells and KC exhibits the same trend as AUC in immune cells for all polyplex micelles.

The dark regions characterize the sinusoids between hepatocytes, where the latter exhibit well-defined NAD(P)H autofluorescence. The previously established automated image analysis algorithm [53,54] adapted to the situation at hand (Supplementary Information III), calculated the retention profile of each polyplex micelle in the sinusoids. The AUC value over a time duration of 45 min indicated that EN15 with high CCR exhibited a long-circulating time in the bloodstream. EN60 showed a shorter plasma half-life, implying a higher uptake of this polyplex micelle by circulating immune cells and KC, in line with the results in Fig. 4f. EN29 and EN76 show an even shorter plasma lifetime. We further calculated the half-life of polyplex micelles through the kinetic curve in sinusoids (Fig. 4g). EN15 with higher CCR was found to have the most prolonged half-life compared to the other polyplex micelles, confirming the lower uptake of EN15 in KC and circulating immune cells (Fig. 4h).

After time-lapse imaging, we performed a co-staining experiment by injecting fluorescein isothiocyanate (FTIC)-labeled F4/80 antibodies to deliver proof of the detected KC's nature that uptake of the micelles (Fig. 5c). FITC-F4/80 antibody-stained Kupffer cells and NAD(P) H-rich hepatocytes take up the micelles differently. Colocalization between Cy3-siRNA polyplex micelles (magenta) and KC (green) is visible in all polyplex micelles, indicating the uptake of polyplex micelles by KC. However, a significant difference in the degree of colocalization was observed. EN60 showed the most uptake by KC, followed by EN76 and EN15. EN29 displayed the most negligible accumulation in KC (Fig. 5c, red▲).

To confirm these results, we investigated the elimination of EN15 and EN76, which showed the most significant difference in IVM, by episcopic imaging of whole mouse cryo-sections [55]. A Cy5-labeled siRNA (Cy5-siRNA) was used to prepare polyplex micelles with both diblock copolymers because the Cy3 fluorescence spectrum overlaps with autofluorescence originating from the stomach and intestine. Mice received an intravenous injection of the micelles before they were euthanized after 15 or 45 min. The cryopreserved mouse mounts were sectioned into the thorax, upper, and lower abdomen. A minimum of 15 tissue slices per section were obtained with a thickness of 100 μm per slice. Sequential RGB illumination (Fig. 6a) and an optimized fluorescent light path that captured the Cy5-siRNA fluorescence visualized the siRNA distribution. Cy5 fluorescence intensity quantification revealed that EN15 was eliminated through both the hepatobiliary and renal routes. However, the Cy5 fluorescence in liver tissue was low compared to the fluorescence in the gallbladder and intestine. This difference is a consequence of the distribution of micelles in a large liver mass during biotransformation.

When they are eliminated hepatobiliary, the Cy5 fluorescence gathers in the bile and intestine (Fig. 6b). A substantial increase in the Cy5 fluorescence signal was also observed in the kidney and urinary bladder over time. Compared to the strong signal in the other organs, the Cy5 fluorescence signal was barely observed in other MPS-rich organs, such as the spleen and lung tissue, when injecting EN15 (Fig. 6c).

In contrast, EN76 exhibits only a minor accumulation in the hepatobiliary system (liver, gallbladder, intestine) and no elimination through the renal system and spleen (*i.e.*, kidney and urinary bladder) (Fig. 6b and c). Therefore, a relatively homogenous increase in fluorescence intensity in most tissues is observed in the images (Fig. 6b), supporting IVM observations that EN76 is rapidly captured by circulating and tissue-resident immune cells. Furthermore, the fluorescence intensity ratio between the liver and the kidney for EN15 and EN76 at 15 min and 45 min further supports the results that EN15 was preferably eliminated by the hepatobiliary clearance pathway (Figure SI 6).

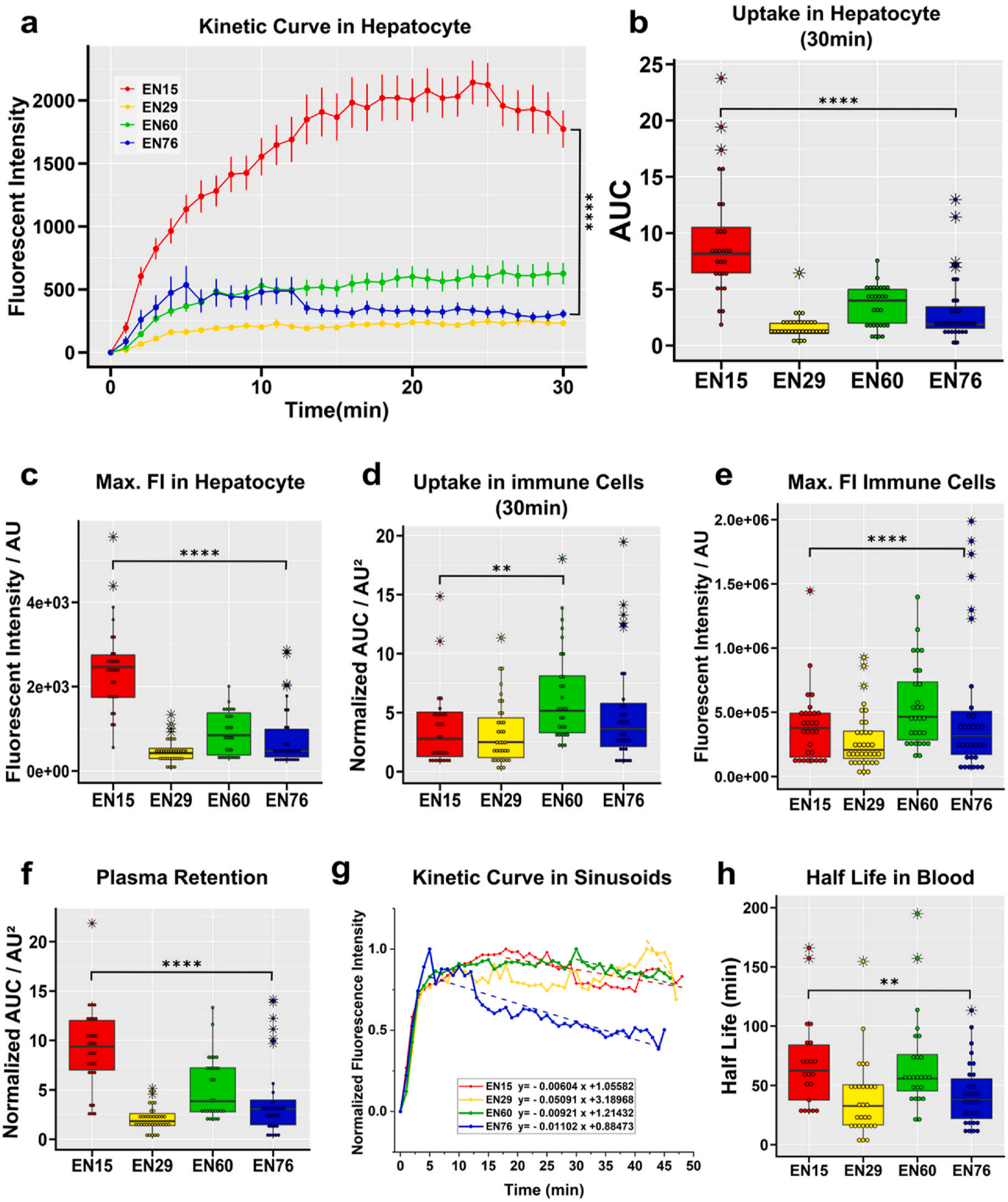

Fig. 4. The CCR controls the passive targeting of oligonucleotide complexes to hepatocytes or the liver mononuclear phagocyte system. Quantifying fluorescence intensity in each cell type from intravital microscopy images was performed by quantitative automated image analysis (Supplementary Information III) (a) The kinetic curve of Cy3-siRNA signal over 30 min in hepatocytes. Data are depicted as mean ± SE. (b) Quantifying the area under the curve (AUC) of the Cy3-siRNA signal within 30 min after injection represents the total accumulation of polyplex micelles in hepatocytes. (c) Maximal Cy3 fluorescence intensity in hepatocytes. The maximal fluorescence intensity was reached after roughly 30 min. (d) AUC of the Cy3-siRNA signal calculated in KC and circulating immune cells within 30 min after injection depicts the uptake of the polyplex micelles in Kupffer cells. (e) Maximal Cy3 fluorescence intensity in KC and circulating immune cells. (f) The plasma retention of Cy3-siRNA micelles is given as the area under the curve (AUC) over 45 min by analyzing the fluorescence intensity in the vein (dark region). (g) The normalized fluorescence intensity in a vein over 45 min. (h) Half-life ($t_{1/2}$) of each polyplex micelles in blood. At least 5 positions (area of 425 μm^2 each) in each mouse's liver were analyzed from 5 mice per group. The number of replicates of all experiments is presented in Table SI 4. All experiments were performed at least three times in duplicates. The significant test is performed using the Pairwise Wilcoxon (Rank Sum) Test with a Benjamini Hochberg p-value adjustment to correct the multiple testing. Significance levels, $^{**}p < 0.01$ and $^{****}p \leq 0.0001$. The exact significant values between each sample group are plotted in Supplementary Information I, Figure SI 5. N/P ratio of 5 was used for micelles in the experiments.

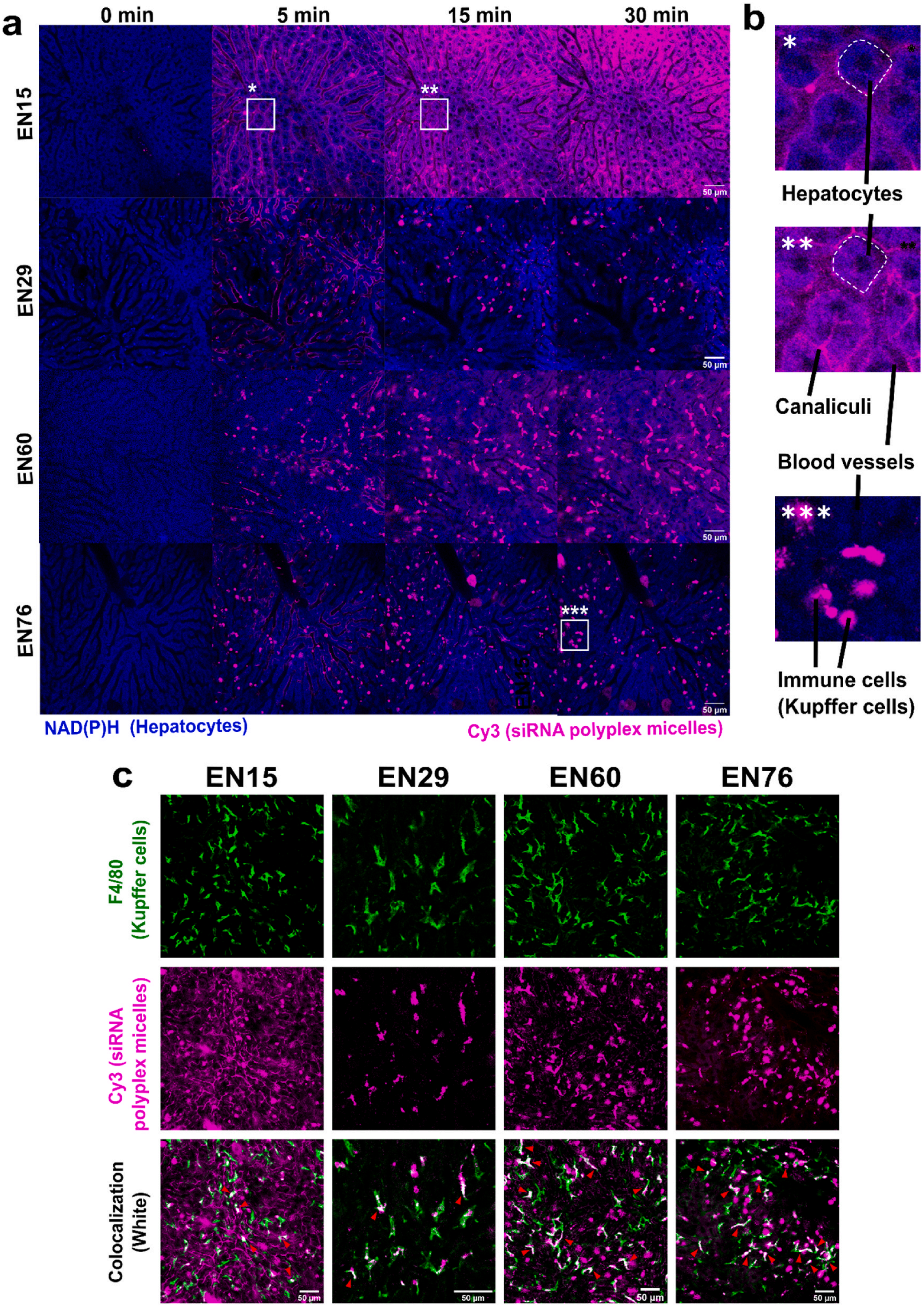

Fig. 5. Different corona-core ratio (CCR) of siRNA polyplex micelles significantly influences the biodistribution profiles. (a) Intravital microscopy of the liver. Hepatocytes are identified by their strong NAD(P)H autofluorescence (blue). Each polyplex micelles were complexed with Cy3-siRNA (magenta) and injected through a tail vein catheter. A representative set of images from a time series (0 min before injection to 30 min after injection) is presented. (b) Magnification of some representative aerials in the images, depicting hepatocytes, blood vessels (sinusoids), the post-hepatocellular canaliculi (indicating elimination of Cy3), and immune cells, in particular, Kupffer cells (local macrophages), (c) F4/80-FITC (green) antibody was injected after IVM evaluation to counterstain Kupffer cells. Colocalization (white) between Cy3-siRNA polyplex micelles (magenta) and Kupffer cells (green) was observed (red ▲). An N/P ratio of 5 was used for micelles in the experiments. (For interpretation of the references to colour in this figure legend, the reader is referred to the Web version of this article.)

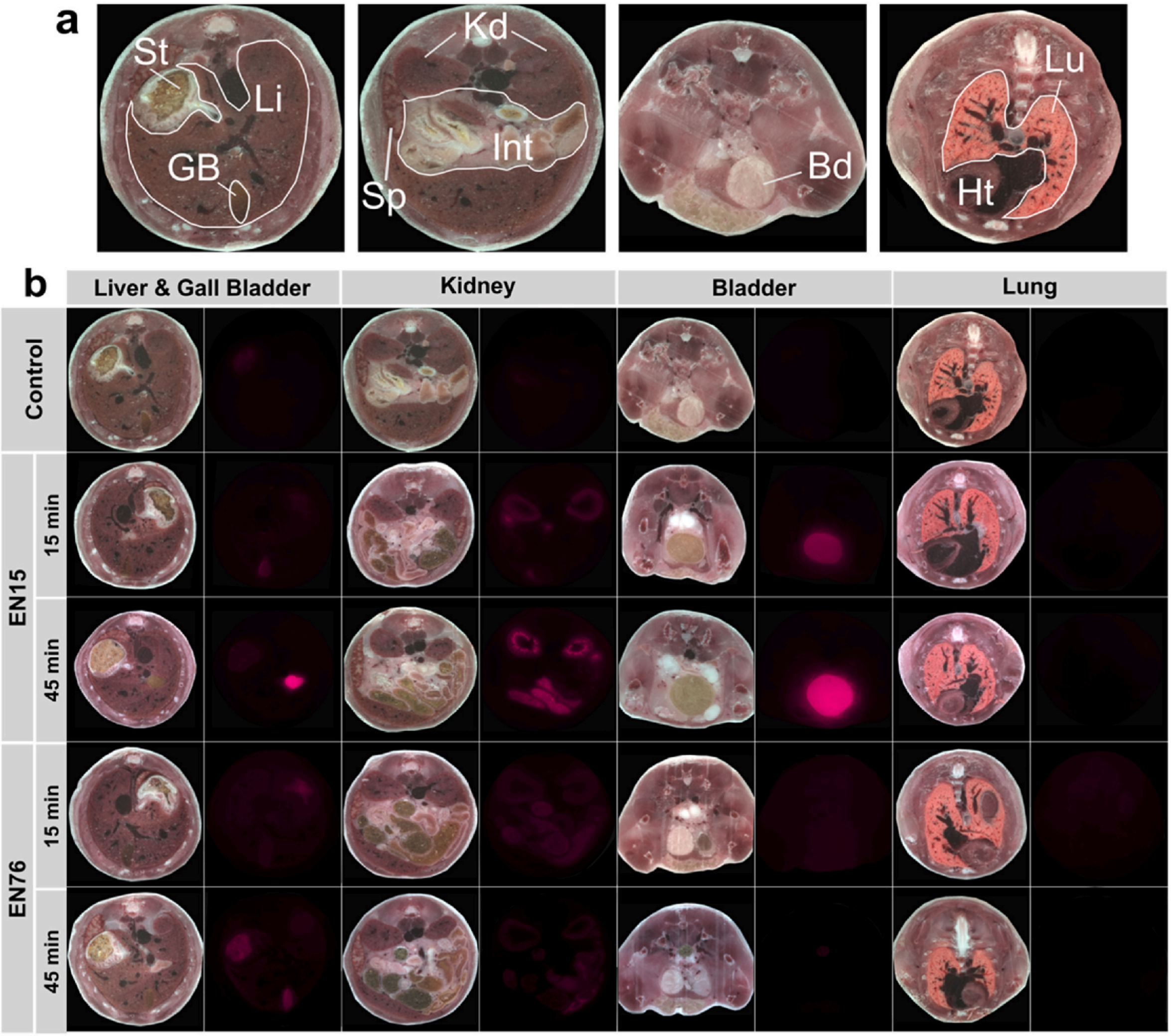

Fig. 6. The CCR affects the clearance pathway of siRNA polyplex micelles. (a) Representative episcopic anatomical RGB-images of different mouse cryo-sections with annotation of St: stomach, Li: Liver, GB: Gallbladder, Kd: Kidney, Int: intestines, Sp: Spleen, Bd: bladder, Lu: lung, Ht: heart (b) Cross-sectional anatomical RGB and full fluorescence images of different mice section from cryo-imaging. EN15 and EN76 prepared with Cy5-siRNA are injected through a tail vein catheter. Mice were euthanized at 15 and 45 min after injection of the siRNA polyplex micelles. The accumulation profile of the Cy5-siRNA polyplex micelles in different organs is identified by the Cy5 fluorescence signal (magenta). (c) Cy5 fluorescence intensity analysis of major organs involved in the sequestering and excretion of nanocarriers: (1) Hepatobiliary clearance pathway (liver, gallbladder, intestine). (2) Renal clearance (kidneys, urinary bladder). (3) sequestering by cells of the adaptive immune system (spleen). AU represents an arbitrary unit of mean fluorescence intensity (FI). All experiments are performed at least three times in duplicates. The significant test is performed using the Pairwise Wilcoxon (Rank Sum) Test with a Benjamini Hochberg p-value adjustment to correct the multiple testing. Significance levels, ****$p \leq 0.0001$. The exact significant values between each sample group are plotted in Supplementary Information I Figure SI 5. An N/P ratio of 5 was used for micelles in the experiments.

3. Discussion

After the self-assembly of block copolymers, polymeric micelles reflect promising nanocarrier systems for gene delivery. Their delivery efficiency strongly depends on the physicochemical properties of nanocarriers that determine the interaction with local tissue environments. A long-circulating time, which indicates low recognition and slow clearance by immune-competent cells, liver, and kidneys, is a feature that characterizes delivery efficiency [56]. The surface properties of nanocarriers, including size, charge, and shape, determine the circulation profile, and targeting moieties may further increase recognition and drug delivery to target cells or tissues [57]. The physicochemical factors that determine an *in vivo* circulation time may vary depending on the type of carrier. Particularly ionic interactions in micelles are critical in influencing *in vivo* biodistribution. The power of such effects is crucial for the formulation and translation of polymeric micelles. It might even be explored to achieve passive targeting based on conformational effects that result from varying protein adsorption to the nanocarrier (protein-corona) [58]. Nanocarriers with unfavorable properties frequently end up in the liver. Thus, targeting the liver is often considered an easy-to-reach goal. Nanocarriers are commonly recognized in the liver by the immune-competent Kupffer cells and LSEC, which shield the hepatocytes from pathogens and nanocarriers [59]. Selective targeting of hepatocytes located behind this potent reticuloendothelial barrier still generates challenges. Thus, targeted nanoformulations for hepatocytes are worth investigating.

Nevertheless, a broad range of inherited devastating metabolic diseases, including porphyrias [60] or hypercholesterinemia [61], to name but a few, reflect a substantial medical need and can principally be tackled by gene delivery to hepatocytes but not the MPS [62]. Consequently, we herein introduce a PEG-*b*-PAGE$_{NH2}$ diblock copolymer consisting of a PEG corona known to increase circulation time by

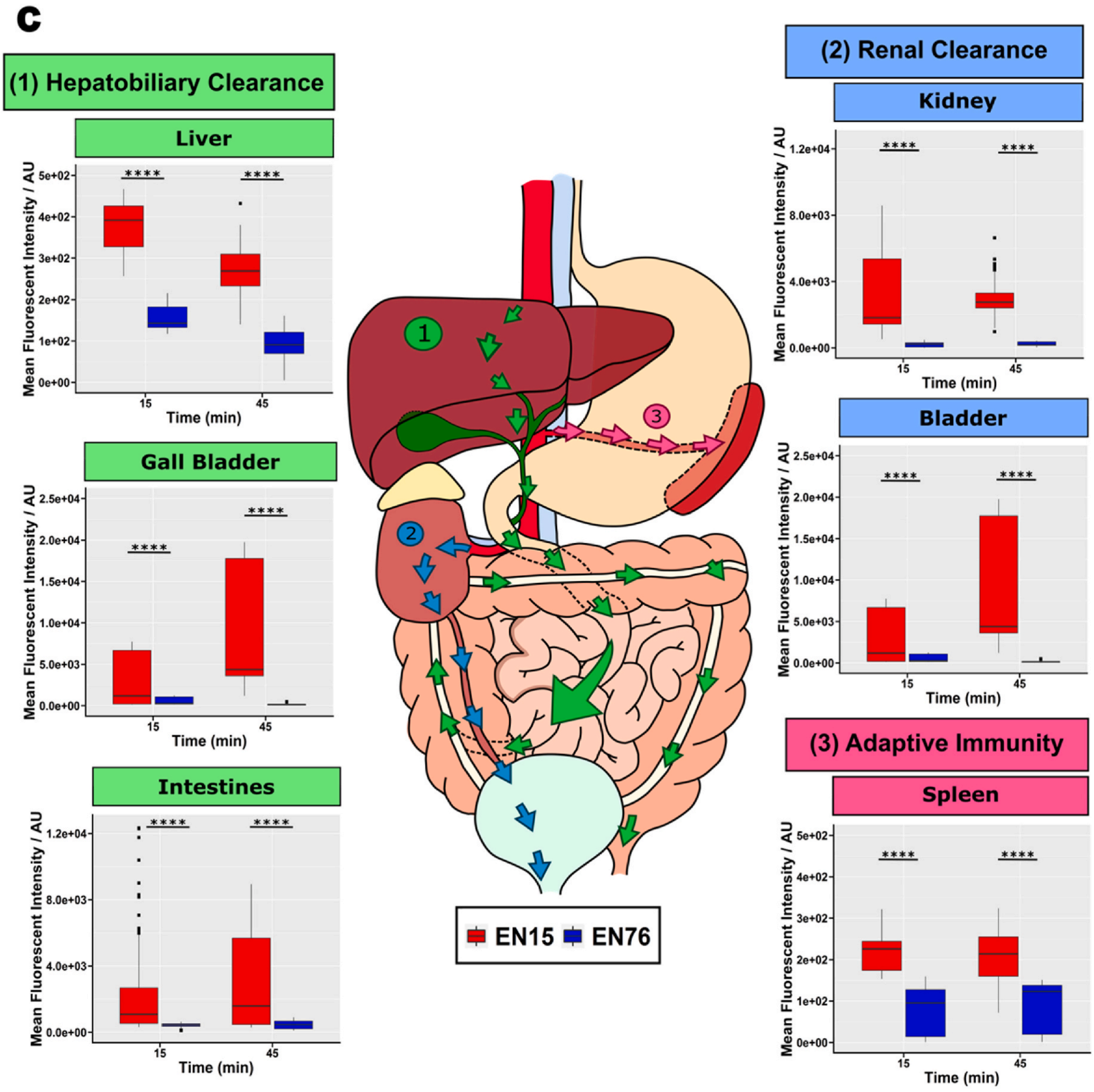

Fig. 6. (*continued*).

lowering protein absorption and cellular recognition density-dependently [63], and a PAGE segment functionalized with NH_2 groups that allow complexation with siRNA resulting in polyplex micelles. We selected four diblock copolymers (EN15_Poly, EN29_Poly, EN60_Poly, EN76_Poly) with PEG consisting of 42 repeating units and modified PAGE with different degrees of polymerization of 15, 29, 60, and 76. This variation results in different ratios of corona (PEG)length to core (PAGE) length that translates into different PEG surface densities. The hydrodynamic diameter of all polyplex micelles (71 nm for EN15, 60 nm for EN29, 104 nm for EN60, and 101 nm for EN76) is below the reported sinusoidal fenestration in the liver of 150–175 nm [64,65]. Among all the polyplex micelles, EN29 with the intermediate CCR was found to be the smallest size among the polyplex micelles. The other research work also observed this phenomenon of increases in polyplex micelles' sizes at both the low and high end of the PEG ratio [66–68]. Petersen et al. observed that the PEG block on the PEG-PEI chain helps to enhance the condensation of nucleic acid, forming smaller and compact spherical polyplex micelles (150 nm–60 nm). They observed a decrease in the zeta potential, since not all amine groups are anymore participating the nucleci acid complexation. In this study, all micelles are complexed at the same N/P ratio of 5, and thus with a similar number of positively charged amine groups. Notably, a trend of increasing zeta potentials for micelles prepared from polymers with a larger core block and lower CCRs. This trend indicates, in line with the presented simulations, with less dense PEG shell, a higher exposure of amine groups towards the surface that does not participate in the complexation of the siRNA and thus increase zeta potential. Also, decreasing the Mw of PEG leads to larger and less compact complexes, while with a highly dense PEG shell, the polyplex micelles' sizes increase (60 nm–130 nm) and form a fluffy and diffuse structure [68]. Farkas et al. and Kunath et al. presented the same trend in size variation with different PEG ratios in siRNA-encapsulated polyplex micelles [66,67]. A larger particle size was observed at lowest PEG ratio (EN76 in this case) and excess PEG (EN15). The bigger hydrodynamic diameter of EN15 may be resulted from the steric repulsive effect of the PEG chain on the shell due to the higher crowdedness of PEG on EN15 if compared to EN29 [39,68]. The lower CCR in EN76 is not able to effectively condense the siRNA, showing rather a looser polyplex micelles with a larger core (TEM) as compared to other micelles with the compact core around 60 nm.

Raman spectral signature of the micelles was used to characterize the cargo-carrier-systems further. The Raman peak position and the intensity of the molecular vibration are sensitive to the change in polarizability, which is influenced by the molecular arrangement and orientation in a given medium. Hence a given Raman peak is characteristic of a given molecular bond and the macromolecule orientation. Therefore, the relative ratio of the Raman peak intensities within one sample can provide information about the molecular structure of macromolecules within a nanocarrier [36]. In our model system of the diblock copolymer-formed polyplex micelles, the ratio of relative Raman peak areas of the PEG (843 cm^{-1}) and PAGE block (646 cm^{-1}) reflects the theoretical ratio of the corona to core molecular weight (CCR). DPD simulations previously applied to investigate multicompartmental micellar structures [69,70] show different micellar conformation of EN15, EN29, EN60, and EN76. Those differences can be confirmed with the experimental findings using Raman fingerprints of the different micelles combined with unsupervised principal component analysis. EN15 and EN29 have a stable core-shell structure with a continuous PEG corona and a compact PAGE-complexed siRNA core. This relatively optimal complexation facilitates stealth properties against Kupffer cells and circulating immune cells (Fig. 3b, d, and 4d).

Further, it resulted in prolonged plasma retention. EN60 depicted a complete but thinner PEG layer in DPD simulation which already resulted in higher KC uptake similar to EN76 (Fig. 3f, h, and Fig. 4d). In contrast, the DPD simulation result of EN76 suggests that the PAGE core with siRNA breaks with the integrity of the PEG corona and may result in possible exposures of some part of the siRNA molecules to the surface of the micelles, increasing their recognition by immune cells and nuclease attacks in the bloodstream. It is important to note that the simulation results for EN76 only suggest a possibility of siRNA molecules located relatively close to the corona in EN76 (low CCR), which experimentally neither translated into an unsuccessful complexation nor reduced the transfection efficacy (Fig. 3g and h). Gel retardation and EtBr assay support a stable complexation of all polymers with siRNA in an aqueous solution (Figure SI 2a, b). All polyplex micelles remained intact after storage of 7 days at 21 °C, followed by 3 h of 10% serum incubation at 37 °C. While free siRNA was, as expected, sensitive to serum RNase-mediated degradation, polyplex micelles remained intact and able to protect their delicate siRNA cargo successfully, indicating the stability and integrity of the micelles (Figure SI 7).

Surface properties, size, and shape of nanocarriers for DNA or RNA affect *in vitro* cellular uptake ability and gene expression/interference [22,28,33]. The intact shielding of EN15 with a high CCR exhibits a lower uptake in comparison to EN29, EN60, and EN76 with relatively low CCR. Consequently, the reduced *in vitro* gene silencing in EN15 are present compared to other micelles. Gene silencing is a multi-step process that involves the efficient crossing of hydrophilic siRNA into the cell, the loading of the siRNA on the RNA-induced silencing complex (RISC), and further cutting the siRNA's target mRNA. Thus successful silencing through the complexation with the different micelles indicates their ability to carry their siRNA cargo over a cellular membrane and release it in the cytosol, making it available for RISC loading [71,72]. An average of 50% of down-regulated mRNA expression from EN15 transfected cells over the three different time points have proven sufficient ability of EN15 in cell internalization, endosomal escape, siRNA release, and interference (Fig. 2c).

However, *in vitro* studies cannot explain the uptake ability and accumulation profile of nanocarriers in the liver during systemic administration. Therefore, we further investigated the pharmacokinetics and distribution profiles in animal models with the proven functionality of all polyplex micelles with varied CCR *in vitro*. Intravital microscopy of the liver confirmed our hypothesis that EN15 preferentially accumulates in hepatocytes with higher PEG-corona density. In contrast, EN60 and EN76 with a lower CCR were captured by Kupffer cells and other circulating immune cells. Even though EN29 showed a lower uptake in KC and other circulating immune cells, the plasma retention profile of EN29 in liver sinusoids was not as high as EN15 and EN60 (Fig. 4f). Intravital microscopy was only performed on the liver, revealing the *in vivo* biodistribution profile of different polyplex micelles in various liver cells. The plasma retention profile was calculated by quantifying the fluorescence intensity in liver blood vessels over 30 min. The smallest size of EN29 (Table 1) among all the polyplex micelles may favor the uptake of EN29 by renal clearance and unspecific recognition by extrahepatic cells. Thus, a lower blood retention profile of EN29 was observed in liver sinusoids, further reducing the possibility of being taken up by hepatocytes and immune cells in the liver (Fig. 4 a-e). Even though EN76 (0.13) has a similar CCR to EN60 (0.16), the lower CCR of EN76 still presented a lower uptake in hepatocytes and blood retention profile. Those effects further demonstrate the importance of CCR in affecting the *in vivo* biodistribution profile. Slightly reducing the CCR from 0.16 to 0.13 (EN60 to EN76), the PEG corona shell of the polyplex micelles loses the integrity to encapsulate the cargo (siRNA) (Fig. 3 h, EN76). The possible exposure of siRNA on EN76 increases the recognition by immune cells in the entire body, not only by the KC and the circulating immune cells in the liver. Thus, the cellular uptake of EN76 in KC and circulating immune cells in the liver and their blood retention profile are lower than EN60 (Fig. 4d, f). Among all the polyplex micelles, EN15 with high CCR possessed significantly longer plasma retention and half-life in the liver sinusoid. The plasma retention results again pinpointed the importance of adequate PEG stealthiness in altering the blood circulation profile of polyplex micelles [28]. Further investigation of the clearance pathway revealed a preferably hepatobiliary clearance for higher CCR micelles, confirming the passive accumulation of these micelles.

To better evaluate the effect of CCR on biodistribution, we simplified the nanocarrier system without any additional modifications as extensively applied in other siRNA carrier systems, such as endosomal escape [22], cholesterol stabilized siRNA used in enhancing interference, conjugation of ligands for better cell-type targeting ability [35,73]. Even though *in vitro* experiments showed significant cellular uptake and gene interference, the systemically administered nanocarriers into the body to express their therapeutic effect further is complicated and requires more investigations on other physicochemical properties of nanocarriers to apply them for *in vivo* silencing prospectively. Nevertheless, the present findings support polyplex micelle design regarding surface modification and functionality. Moreover, the established spectroscopy and simulation techniques for CCR analysis may assist researchers in evaluating the corona stealth properties *in silico*.

4. Conclusion

The corona-core ratio (CCR) of polymeric micelles generated through polyion complexation is experimentally accessible by Raman spectroscopy, reflects the molecular weight ratios of both polymer blocks, and is supported by *in silico* simulations. Our data suggest that purposeful modification of CCR may be applied for targeting specific cells and tissues and may be used to modify the properties of the carrier, allowing the formation of a stable PEG corona. The latter was confirmed to shield polyplex micelles from nonspecific uptake *in vitro* and *in vivo*, leading to a passive accumulation in hepatocytes while avoiding local and systemic clearance by the mononuclear phagocyte system.

5. Material & methods

5.1. Materials

Poly(ethylene glycol) monomethyl ether (M_n of PEG_{42} = 2000 g mol^{-1}), NaH (95%), CaH_2 (95%), 2,2-dimethoxy-2-phenyl acetophenone (99%, DMPA), and allyl glycidyl ether (99%, AGE) were purchased from Sigma Aldrich (Merck KGaA, Darmstadt, Germany). Allyl glycidyl ether was dried over CaH_2 and distilled under reduced pressure before being used in the anionic polymerization. Cysteamine hydrochloride (98%) was obtained from Carbolution Chemicals (Sankt Ingbert, Germany). Potassium hydride (KH) was purchased from Acros Organics (ThermoFisher Scientific, Darmstadt, Germany), purified by washing with dry cyclohexane under an argon atmosphere, and dried in a vacuum. All deuterated solvents for NMR measurements were obtained from Deutero (Kastellaun, Germany). Regenerated cellulose membranes (Spectrum Labs™ Spectra/Por® 6 pre-wetted dialysis tubing) with a nominal molecular weight cut-off of 1 kDa from Spectrum Laboratories, Inc. Were used to purify polymers *via* dialysis. All single-strand oligonucleotides are provided by Eurofins Genomics (Ebersberg Germany) (Table 2). In-house annealing was done by dissolving the single-stranded oligonucleotides into 1 mmol L^{-1} with 5X annealing buffer containing 300 nmol L^{-1} KCl, 30 nmol L^{-1} Hepes, and 2 mmol L^{-1} MgCl$_2$. 10 μl of sense oligonucleotide was annealed with 10 μl of antisense oligonucleotide by adding 4 μl annealing buffer. The mixed solution was heated at 90 °C for 1 min, followed by 1-h incubation at 37 °C. The annealed oligonucleotide was then diluted to the desired concentration for micelles preparation. Materials required in cell culture are Dulbecco's Modified Eagle's Medium (DMEM, Gibco), fetal bovine serum (FBS, ThermoFisher Scientific, Darmstadt, Germany), Penicillin Streptomycin Solution (Gibco, Thermo Fisher Scientific, Darmstadt, Germany).

5.2. *Preparation of PEG$_{42}$-b-PAGE$_{NH2}$*

The preparations of PEG$_{42}$-*b*-PAGE by anionic ring-opening polymerizations were carried out in a Braun UNIlab Pro SP Workstation (M. Braun Inertgas-Systeme GmbH, Munich, Germany) under an argon atmosphere. Poly(ethylene glycol) (2000 g mol^{-1}, approx. 500 mg) was melted at 110 °C and deprotonated with a spatula tip of sodium hydride (approx. 1.2 eq.). Allyl glycidyl ether (AGE) was added after 2 h, and the mixture was stirred for 24 h. The polymerization was quenched by adding MeOH (0.5 mL) and cooled to room temperature. The crude polymer was dried in a vacuum at 100 °C to afford PEG$_{42}$-*b*-PAGE [74]. ^{1}H NMR (250 MHz, CDCl$_3$): δ = 6.0–5.8 (-OCH$_2$C*H*═CH$_2$), 5.4–5.1 (-OCH$_2$CH═C*H*$_2$), 4.1–3.9 (-OC*H*$_2$CH═CH$_2$), 3.8–3.3 (polymer backbone). ^{13}C NMR (63 MHz, CDCl$_3$): δ = 70.2, 72.4, 78.9, 117.1, 135.1 ppm (Table SI 1).

The functionalization of PEG$_{42}$-*b*-PAGE prepared the polycations PEG$_{42}$-*b*-PAGE$_{NH2}$ for the complexation of oligonucleotides with primary amines *via* thiol-ene click reaction. PEG$_{42}$-*b*-PAGE (approx. 200 mg), cysteamine hydrochloride (3.0 eq.), and 2,2dimethoxy-2-phenyl acetophenone (0.3 eq.) were dissolved in a 1:2 mixture of tetrahydrofuran (THF) and methanol (MeOH). The solution was degassed by flushing with Ar for 10 min and irradiated with UV light for 2 h under stirring. UV irradiations were carried out in a UVACUBE 100 equipped with a 100 W mercury lamp (Dr. Hönle AG, Gräfelfing, Germany). The polymer was purified by dialysis against THF, a 1:1 mixture of THF and water, and finally, water to afford PEG$_{42}$-*b*-PAGE$_{NH2}$ after freeze-drying using an Alpha 1–2 LDplus device (Martin Christ Gefriertrocknungsanlagen GmbH, Osterode am Harz, Germany). ^{1}H NMR (250 MHz, MeOD-*d*$_4$) δ = 3.8–3.4 (polymer backbone), 3.25–3.1 (-C*H*$_2$-NH2), 2.95–2.8 (-S-C*H*$_2$-CH$_2$-NH$_2$), 2.8–2.6 (-C*H*$_2$-S-), 2-1.8 (-C*H*$_2$-CH$_2$-S-) ppm (Table SI 2).

5.3. *Size exclusion chromatography*

Size exclusion chromatography (SEC) analysis of PEG$_{42}$ -*b*-PAGE was performed in chloroform on a Shimadzu system equipped with an LC-10AD VP pump, a RID-10A detector, and a PSS SDV guard/linear S (5 μm particle size) column. A 94:2:4 mixture of chloroform, isopropanol, and triethylamine was used as eluent, and a flow rate of 1 mL min^{-1} at 40 °C was applied. The system was calibrated with poly(ethylene glycol) standards from PSS (M$_n$ = 1470–42000 g mol^{-1}). Size exclusion chromatography (SEC) analysis of PEG$_{42}$-*b*-PAGE$_{NH2}$ was performed in dimethylacetamide (DMAc) on an Agilent 1200 series equipped with a G1310A pump, a RID G1362A detector, and a PSS GRAM guard/1000/30 Å (10 μm particle size) column. DMAc with 0.1 g L^{-1} of lithium chloride as an additive was used as an eluent, and a flow rate of 1 mL min^{-1} at 40 °C was applied. The system was calibrated with poly(ethylene glycol) standards from PSS (M$_n$ = 440 to 969 700 g mol^{-1}).

5.4. *Nuclear magnetic resonance spectroscopy*

^{1}H NMR and proton decoupled ^{13}C NMR spectra were measured on a Bruker Avance I spectrometer (250 MHz) at 298 K. The chemical shifts are given in ppm and were referenced to the residual solvent signals.

5.5. *Cell culture*

Hela cells were cultured in cell culture flasks at 37 °C at 5% CO$_2$ (HeraCell CO$_2$ Incubator, Heraeus, Germany). Dulbecco's Modified Eagle's Medium (DMEM, Gibco) with 10% fetal bovine serum (FBS, ThermoFisher Scientific, Darmstadt, Germany) and 1% Penicillin Streptomycin Solution (Gibco, Thermo Fisher Scientific, Darmstadt, Germany) was used as a culture medium. Cells were passed at approximately 70% confluency by trypsinization.

5.6. *Preparation of polyplex micelles*

siRNA encapsulated polyplex micelles were prepared by polyion complexation. Polyplex micelles were prepared with the same amount of siRNA for every polymer. Therefore, each polyplex micelles contained the same concentration of siRNA. All polymers were dissolved at 1 mg mL^{-1} for *in vitro* and 10 mg mL^{-1} for *in vivo* experiments. siRNA solution containing 200 ng μL^{-1} was prepared in nuclease-free water. Polyplex was generated by fast mixing of the polymer solution with siRNA solution at N/P ratio 5 (N/P ratio is defined as the residual molar ratio of amine (N) groups of polymers to the phosphate (P) groups of siRNA). The polyplex micelles used in all *in vitro*, *in vivo*, and physical properties characterization (TEM, RAMAN, DLS) are complex at N/P ratio 5.

5.7. *Gel retardation assay*

A polyplex micelle with a final siRNA concentration at 20 ng μL^{-1} was formed at different N/P ratios in 20 μL water. Polyplex micelles were stabilized by incubation at 4 °C for 15 min. Agarose gels (2% w/w) were prepared by using 1X Tris-acetate-EDTA (TAE) buffer (Thermo Fisher Scientific, Darmstadt, Germany), consisting of 40 mmol L^{-1} Tris, 20 mmol L^{-1} acetic acids, 1 mmol L^{-1} EDTA. Polyplex micelles with different N/P ratios were loaded into a pre-prepared agarose gel. In addition, a 100 bp DNA marker (Zymo Research GmbH, Freiburg im Breisgau, Germany) and naked siRNA (20 ng μL^{-1}) were loaded as a size indicator and control. Electrophoresis was carried out at 100 V using Owl Horizontal Electrophoresis Systems (ThermoFisher Scientific, Darmstadt, Germany). After 45 min, the gel was examined under an ultraviolet gel documentation system (Syngene, Maryland, USA) to visualize the migrated siRNA bands.

5.8. *Stability test*

Polyplex micelles loaded with a 22 bp siRNA (N/P ratio 5) at 20 ng μL^{-1} were incubated in RNase-free 10 mmol L^{-1} HEPES buffer (pH 7.4) for 7 days at 21 °C. The micelles were incubated with 10% human serum or sterile 10% Krebs Henseleit Buffer (KHB), imitating the blood's ion composition for 3 h at 37 °C and rocking to test the stability of the 7 days old materials. After 7 days, the samples were split into two halves. One portion was directly subjected to a gel retardation assay (GRE; 1.5% Agarose, 100 V, 45 min, in TAE-Buffer). Another half of the samples were heated at 95 °C for 5 min and mixed with an acidic 6x concentrated gel loading dye (pH 4.2), destroying the micelles and releasing the siRNA. Gel retardation assay was performed with the method mentioned before.

5.9. Ethidium bromide assay

20 ng μL^{-1} of siRNA solution was pre-incubated with 0.4 μg mL^{-1} ethidium bromide (EtBr) at 4 °C for 15 min. In the above-mentioned micelles preparation method, EtBr containing siRNA solution was used to prepare polyplex micelles with a constant final siRNA concentration of 10 ng μL^{-1} at different N/P ratios. Prepared polyplex micelles were incubated at 4 °C for 15 min. The fluorescence intensity of EtBr in polyplex micelles solution was measured on a fluorescence microplate reader (EnSpire, PerkinElmer, Hamburg, Germany) with a dichroic filter at excitation and an emission wavelength of EtBr ($\lambda_{Ex,\ max}$ = 530 nm, $\lambda_{Em,\ max}$ = 600 nm). The fluorescence intensity of each polyplex micelles was normalized with the fluorescence intensity from EtBr intercalated siRNA solution (10 ng μL^{-1}) without polymers.

5.10. Dynamic light scattering and zeta potential

All polyplex micelles were prepared in Type 1 water at 200 ng μL^{-1}. The hydrodynamic radius and zeta potential of all polyplex micelles were determined by Zetasizer Nano ZS (Malvern Instruments, Herrenberg, Germany). All solutions were equilibrated for 180 s at 25 °C before measurement. The dynamic light scattering (DLS) measurements were conducted for 3 × 20 runs (10 s per run) with a 633 nm light source and a detection angle of 173°. The data were analyzed using a cumulative method to determine the mean hydrodynamic diameter and polydispersity index (PDI) [75]. The zeta potential was measured *via* the M3-PALS technique using disposable capillary cells (DTS1061, Malvern Instruments, Herrenberg, Germany).

5.11. Transmission electron microscopy

Polyplex micelle solutions were dropped onto Quantifoil grids (Quantifoil, Jena, Germany, R2/2), and excess solutions were removed by the filter, leaving a thin layer of polyplex micelles solution. Finally, the grid was transferred to FEI Tecnai G^2 20 system (ThermoFisher Scientific, Darmstadt, Germany) for imaging at an acceleration voltage of 200 kV.

5.12. Reverse transcriptase quantitative PCR

The gene silencing ability of each polyplex micelle was studied using reverse transcriptase quantitative (RT-q) PCR with toll-like receptor 4 (*TLR4*, NM_138554.4) as the target gene. HeLa cells were seeded into 24-well plates (50 000 cells per well) in a culture medium (DMEM containing 10% FBS and 1% Penicillin Streptomycin Solution) and incubated for 24 h. Cells were transfected with TLR4 siRNA (siTLR4) loaded polyplex micelles in Opti-MEM reduced serum media at a 200 nmol L^{-1} siRNA concentration and an NP ratio of 5. Transfected cells were harvested at different time points (12, 24, and 48 h) after transfection. RNA extraction was performed using Direct-zol RNA MicroPrep with TRI Reagent (Zymo Research GmbH, Freiburg im Breisgau, Germany). Reverse transcription and the quantitative PCR were performed using the GoTaq 1-Step RT-qPCR System (Promega, Walldorf, Germany) with the Rotor-gene Q system (Qiagen, Hilden, Germany). *TCF7L2* gene [48,49] was used as an endogenous housekeeping gene. The mRNA expression level was calculated using the comparative C_t method ($2^{-\Delta\Delta Ct}$) [76].

5.13. Lactate dehydrogenase assay

Hela cells were cultured and transfected with polyplex micelles following the protocol described above. The polyplex micelles' cytotoxicity was determined by quantifying the lactate dehydrogenase (LDH) amount in the culture medium after 24 h. The LDH assay was performed using CytoTox96 Non-Radioactive Cytotoxicity Assay kits (Promega, Walldorf, Germany). First, 50 μL of the supernatant medium from the cultured cell was transferred to a 96-wells plate, followed by adding 50 μL of the CytoTox96 reagent. After 30 min of incubation, 50 μL of the stop solution was added to each well. The absorbance signal of LDH was measured at 490 nm in a fluorescence microplate reader (EnSpire, PerkinElmer, Hamburg, Germany). The result was normalized with the maximum LDH absorbance value obtained from 100% cell lysis.

5.14. Cellular uptake

Cells were incubated in 12-well plates for 24 h before the experiment. Polyplex micelles were prepared with Cy3-siRNA ($\lambda_{Ab,\ max}$ = 554 nm, $\lambda_{Em,\ max}$ = 568 nm), allowing the tracking of polyplex micelles and given to the cells (final concentration at 200 nmol L^{-1}). The uptake of the polyplex micelles was evaluated at 1, 4, 12, and 24 h. Transfected cells were washed twice with PBS to remove the remaining polyplexes from the cell surface and solution and detached by flushing them with a 5% EDTA PBS solution. The fluorescence intensity of Cy3 in cells was then quantified by Flow Cytometer BD Accuri C6 Plus (Becton Dickinson, Heidelberg, Germany).

5.15. Raman Spectroscopy

All free polymers, polyplex micelles, and siRNA solutions were prepared in nuclease-free water at a consistent siRNA concentration of 200 ng μL^{-1} at an N/P ratio of 5. Raman spectroscopy of all samples was performed on an upright micro-Raman system (CRM 300, WITec GmbH, Ulm, Germany), exciting the sample 785 nm (200 mW laser power) and detecting Raman signal through a 300 g mm^{-1} grating and a Deep Depletion CCD camera (DU401 BR-DD, ANDOR, 1024 × 127 pixels). Around 1 μL of each sample was dropped onto the CaF_2 substrate for measurement. On each sample, an average of 15 spectra were taken at several positions using a 100× LD Plan-Apochromatic objective NA 0.75 (Carl Zeiss, Jena, Germany) by integrating signals over 0.05 s per spectrum. The raw Raman spectra were preprocessed in GNU R (version 4.0.2) [77] using in-house algorithms. The preprocessing steps involved spectral background correction using a sensitive non-linear iterative peak (SNIP) algorithm [78] and vector normalization. Principal component analysis (PCA) was done using GNU R [77] to visualize the differences between groups. All Raman spectra and PCA plots were plotted using GNU R with ggplot2 plugin [79] and origin software (OriginPro 2019b) [80].

5.16. Molecular dynamic and dissipative particle dynamic simulations

All simulations were performed with the program Materials Studio 2020 (MS) and its modules [81]. The Visualizer and Amorphous Cell modules [82] were applied to construct atomistic models, and the Forcite module [83] was used to optimize the structures. All the above steps were performed with the COMPASSII force field [84]. The Mesocite module [46] was used for DPD simulations, which were carried out using coarse-grained models with beads. The systems simulated in this work were composed of siRNA, PEG_{42}-*b*-$PAGE_{NH2}$ block copolymer, and water. The details of DPD simulations are provided in Supplementary Information II.

5.17. Animals

Experimental animal procedures were approved by the local government authority of Thuringia, Thüringer Landesverwaltungsamt, and performed according to the approved guidelines (UKJ 20-013). For experiments, FVB/N mice were used. All mice were housed under specific pathogen-free environments in the animal facility of the Jena University Hospital with free access to standard rodent chew, acidified, sterile drinking water, and sterile enrichment, under artificial day-night cycles (12 h light-dark cycles) at room temperature of 23 °C and humidity of 30–60%. All experiments were carried out on mixed populations of males and females. Gender-specific effects had not been noted in any experiment.

5.18. Intravital microscopy

FBV/N mice received orally 1–5 mg kg^{-1} body weight $(BW)^{-1}$ Meloxicam (Melosus 0.5 g L^{-1}, CP-Pharma, Burgdorf, Germany) for pain relief. A laparotomy was performed on the left lateral abdomen, and a tail vein catheter was placed under general isoflurane anesthesia after the animal reached the state of surgical tolerance. The liver was gently flattened and fixed onto a cover glass to ensure sufficient exposure area for imaging. Mice were placed on a warm pad (37 °C) throughout the experiment. Intravital microscopy imaging was performed on an LSM-780 (Carl Zeiss, Jena, Germany) with the specification of air-corrected 20x plan-apochromatic NA 0.8 (Carl Zeiss, Jena, Germany). Liver tissue was recognized by NADPH autofluorescence with excitation from 375 nm to 405 nm and emission from 410 nm to 485 nm 1 min after the imaging started, 30 μg polyplex micelles loaded with Cy3-siRNA were administered through a tail vein catheter. Time-lapse imaging was carried out for 45 min at 7 areas of interest. Images were taken using an air-corrected 40× plan-apochromatic objective NA 0.95 (Carl Zeiss, Jena, Germany). Animals were sacrificed by cervical dislocation at the end of the experiment while under general anesthesia.

5.19. Episcopic imaging biodistribution

Mice injected with Cy5-siRNA-loaded polyplex micelles were euthanized after 15 min and 45 min. Mice were frozen postmortem in TissueTek (OCT Compound, Frankfurt, Germany). The episcopic imaging system was set up on a cryo-microtome (CM3050 S Cryostat, Leica Biosystems, Wetzlar, Germany) for cross-section imaging of the whole mouse. Cy5 was excited with a LED at 625 nm wavelength (M625L4, Thorlabs, Newton, New Jersey, USA) and subsequently filtered by a 1″ bandpass filter with a center wavelength of 630 nm and FWHM of 20 nm (ET630/20x, Chroma, Bellows Falls, VT, USA). Cy5 fluorescence was observed through a 2″ bandpass filter with a center wavelength of 670 nm and FWHM of 30 nm (ET670/30 m, Chroma, Bellows Falls, VT, USA). A monochrome camera CCD acquired images with 4500 × 3600 pixels and 6 μm pixel size (MicroLine ML16200, FLI Instruments, Lima, NY, USA) equipped with a 1:1 lens with 89 mm focal length using f/4.8 (XENON-ZIRCONIA 2.8/89, Schneider, Bad Kreuznach, Germany). RGB images were taken by illuminating the sample sequentially with a ring of red, green, and blue LEDs (24 × SK6812RGBW-WS, Opsco, Guangdong, China) [55].

5.20. Statistics

Data processing, analysis, and visualization were done using GNU R version 4.0.2 and higher. The packages and functions used were the following: tidyverse, stringr, purrr, dplyr, concatenate, Rmisc, readr, readxl, grid, hyperSpec, e1071, stats, graphics, cluster, MASS, peaks, klar, ellipse, plotrix, klaR, ggplot2. Images were visualized and analyzed using Fiji distribution of ImageJ 2.0.0-RC-69/1.52p, Inkscape 1.0, and in-house developed software CIAnalyzing version 1.7 © Leibniz-Institute of Photonic Technologies. Statistical significance was investigated by pairwise comparisons using the Wilcoxon rank-sum test since normal distribution and equal variances were not present in all datasets. In addition, if multiple comparisons were calculated on a dataset, the false discovery rate had been controlled by applying the Benjamini-Hochberg procedure [85]. The figure legends and Supplementary Information I (Table SI 4) provide information on the statistical procedures used in each graph.

Credit author statement

WanLing Foo, Concept-ualization, Method-ology, Soft-ware, Vali-dation, Formal analysis, Invest-igation, Resources, Data Curation, Writing - Original Draft, Visuali-zation, Super-vision, Project admin-istration, Funding acquisition, Zoltán Cseresnyés, Method-ology, Soft-ware, Vali-dation, Formal analysis, Invest-igation, Data Curation, Writing - Original Draft, Writing - Review & Editing, Writing - Review & Editing, Project admin-istration, Carsten Rössel, Invest-igation, Data Curation, Writing - Original Draft, Yingfeng Teng, Invest-igation, Writing - Review & Editing, Anuradha Ramoji, Method-ology, Formal analysis, Writing - Original Draft, Writing - Review & Editing, Super-vision, Project admin-istration, Mingzhe Chi, Method-ology, Invest-igation, Writing - Original Draft, Walter Hauswald , Method-ology, Invest-igation, Writing - Review & Editing, Project admin-istration, Funding acquisition, Sophie Huschke, Invest-igation, Visuali-zation, Stephanie Hoeppener, Invest-igation, Writing - Original Draft, Writing - Review & Editing, Visuali-zation, Jürgen Popp, Resources, Funding acquisition, Felix H. Schacher, Method-ology, Vali-dation, Resources, Data Curation, Writing - Review & Editing, Super-vision, Project admin-istration, Funding acquisition, Marek Sierka, Method-ology, Vali-dation, Resources, Data Curation, Writing - Original Draft, Writing - Review & Editing, Super-vision, Project admin-istration, Funding acquisition, Marc Thilo Figge, Method-ology, Soft-ware, Vali-dation, Formal analysis, Invest-igation, Resources, Data Curation, Writing - Original Draft, Writing - Review & Editing, Super-vision, Project admin-istration, Funding acquisition, Adrian T. Press, Concept-ualization, Method-ology, Vali-dation, Formal analysis, Invest-igation, Resources, Data Curation, Writing - Original Draft, Writing - Review & Editing, Super-vision, Project admin-istration, Funding acquisition, Michael Bauer, Concept-ualization, Method-ology, Vali-dation, Resources, Data Curation, Writing - Original Draft, Writing - Review & Editing, Super-vision, Project admin-istration, Funding acquisition.

Declaration of competing interest

The authors declare that they have no known competing financial interests or personal relationships that could have appeared to influence the work reported in this paper.

Data availability

Data will be made available on request.

Acknowledgments

This work was funded by the Deutsche Forschungsgemeinschaft (DFG, German Research Foundation) – project number 316213987 – SFB 1278 PolyTarget (projects C03, Z01, C01, C06, A01, B08). The transmission electron microscopy (TEM) facility of the Jena Center for Soft Matter (JCSM) were funded by the DFG and the European Funds for Regional Development (EFRE). In addition, the authors thank Alexander Wiede (Leibniz Institute of Photonic Technology) for designing and constructing the episcopic imaging system and Sebastian Bierwirth (Leibniz Institute of Photonic Technology) for providing the episcopic imaging analysis software CI Analyzing version 1.7 © IPHT.

Appendix A. Supplementary data

Supplementary data to this article can be found online at https://doi.org/10.1016/j.biomaterials.2023.122016.

References

[1] R. Böttger, G. Pauli, P.-H. Chao, N. Al Fayez, L. Hohenwarter, S.-D. Li, Lipid-based nanoparticle technologies for liver targeting, Adv. Drug Deliv. Rev. 154–155 (2020) 79–101.

[2] P. Byass, The global burden of liver disease: a challenge for methods and for public health, BMC Med. 12 (2014) 159, 159.

[3] P. Marcellin, B.K. Kutala, Liver diseases: a major, neglected global public health problem requiring urgent actions and large-scale screening, Liver Int. 38 (S1) (2018) 2–6.

[4] S.K. Asrani, H. Devarbhavi, J. Eaton, P.S. Kamath, Burden of liver diseases in the world, J. Hepatol. 70 (1) (2019) 151–171.

[5] A. Sehgal, A. Vaishnaw, K. Fitzgerald, Liver as a target for oligonucleotide therapeutics, J. Hepatol. 59 (6) (2013) 1354–1359.

[6] A.T. Press, P. Babic, B. Hoffmann, T. Müller, W. Foo, W. Hauswald, J. Benecke, M. Beretta, Z. Cseresnyés, S. Hoeppener, I. Nischang, S.M. Coldewey, M.H. Gräler, R. Bauer, F. Gonnert, N. Gaßler, R. Wetzker, M.T. Figge, U.S. Schubert, M. Bauer, Targeted delivery of a phosphoinositide 3-kinase γ inhibitor to restore organ function in sepsis, EMBO Mol. Med. 13 (10) (2021), e14436.

[7] M. Bauer, A.T. Press, M. Trauner, The liver in sepsis: patterns of response and injury, Curr. Opin. Crit. Care 19 (2) (2013) 123–127.

[8] D.V. Morrissey, J.A. Lockridge, L. Shaw, K. Blanchard, K. Jensen, W. Breen, K. Hartsough, L. Machemer, S. Radka, V. Jadhav, N. Vaish, S. Zinnen, C. Vargeese, K. Bowman, C.S. Shaffer, L.B. Jeffs, A. Judge, I. MacLachlan, B. Polisky, Potent and persistent in vivo anti-HBV activity of chemically modified siRNAs, Nat. Biotechnol. 23 (8) (2005) 1002–1007.

[9] S. Agarwal, A.R. Simon, V. Goel, B.A. Habtemariam, V.A. Clausen, J.B. Kim, G. J. Robbie, Pharmacokinetics and pharmacodynamics of the small interfering ribonucleic acid, givosiran, in patients with acute hepatic porphyria, Clin. Pharmacol. Therapeut. 108 (1) (2020) 63–72.

[10] K.A. Whitehead, R. Langer, D.G. Anderson, Knocking down barriers: advances in siRNA delivery, Nat. Rev. Drug Discov. 8 (2) (2009) 129–138.

[11] D.M. Bissell, L. Gouya, M. Balwani, D. Rees, P. Stein, U. Stolzel, P.A. Peiro, H. L. Bonkovsky, S. Keel, C. Park, In envision, a phase 3 study of safety and efficacy of givosiran, an investigational rnai therapeutic, in: Acute Hepatic Porphyria Patients, Hepatology, WILEY 111 RIVER ST, HOBOKEN 07030-5774, NJ USA, 2019, pp. 100A–101A.

[12] A. Mullard, FDA approves landmark RNAi drug, Nat. Rev. Drug Discov. 17 (9) (2018) 613, 613.

[13] C. Morrison, Alnylam prepares to land first RNAi drug approval, Nat. Rev. Drug Discov. 17 (3) (2018) 156–157.

[14] S. Simões, A. Filipe, H. Faneca, M. Mano, N. Penacho, N. Düzgünes, M. Pedroso de Lima, Cationic liposomes for gene delivery, Expet Opin. Drug Deliv. 2 (2) (2005) 237–254.

[15] M. Whitemore, S. Li, L. Huang, Liposome vectors for in vivo gene delivery, Current Protocols in Human Genetics 20 (1) (1999) 1–18, 12.18.

[16] A.D. Judge, V. Sood, J.R. Shaw, D. Fang, K. McClintock, I. MacLachlan, Sequence-dependent stimulation of the mammalian innate immune response by synthetic siRNA, Nat. Biotechnol. 23 (4) (2005) 457–462.

[17] V.C. Mosqueira, P. Legrand, J.L. Morgat, M. Vert, E. Mysiakine, R. Gref, J. P. Devissaguet, G. Barratt, Biodistribution of long-circulating PEG-grafted nanocapsules in mice: effects of PEG chain length and density, Pharm. Res. (N. Y.) 18 (10) (2001) 1411–1419.

[18] T.A. Tockary, W. Foo, A. Dirisala, Q. Chen, S. Uchida, S. Osawa, Y. Mochida, X. Liu, H. Kinoh, H. Cabral, K. Osada, K. Kataoka, Single-stranded DNA-packaged polyplex micelle as adeno-associated-virus-inspired compact vector to systemically target stroma-rich pancreatic cancer, ACS Nano 2019 (2019).

[19] C.D. Walkey, J.B. Olsen, H. Guo, A. Emili, W.C. Chan, Nanoparticle size and surface chemistry determine serum protein adsorption and macrophage uptake, J. Am. Chem. Soc. 134 (4) (2012) 2139–2147.

[20] H.C. Fischer, T.S. Hauck, A. Gómez-Aristizábal, W.C.W. Chan, Exploring primary liver macrophages for studying quantum dot interactions with biological systems, Adv. Mater. 22 (23) (2010) 2520–2524.

[21] K. Hayashi, H. Chaya, S. Fukushima, S. Watanabe, H. Takemoto, K. Osada, N. Nishiyama, K. Miyata, K. Kataoka, Influence of RNA strand rigidity on polyion complex formation with block catiomers, Macromol. Rapid Commun. 37 (6) (2016) 486–493.

[22] M. Tangsangasaksri, H. Takemoto, M. Naito, Y. Maeda, D. Sueyoshi, H.J. Kim, Y. Miura, J. Ahn, R. Azuma, N. Nishiyama, K. Miyata, K. Kataoka, siRNA-loaded polyion complex micelle decorated with charge-conversional polymer tuned to undergo stepwise response to intra-tumoral and intra-endosomal pHs for exerting enhanced RNAi efficacy, Biomacromolecules 17 (1) (2016) 246–255.

[23] S. Mao, M. Neu, O. Germershaus, O. Merkel, J. Sitterberg, U. Bakowsky, T. Kissel, Influence of polyethylene glycol chain length on the physicochemical and biological properties of poly (ethylene imine)-graft-poly (ethylene glycol) block copolymer/SiRNA polyplexes, Bioconjugate Chem. 17 (5) (2006) 1209–1218.

[24] C.-Y. Sun, S. Shen, C.-F. Xu, H.-J. Li, Y. Liu, Z.-T. Cao, X.-Z. Yang, J.-X. Xia, J. Wang, Tumor acidity-sensitive polymeric vector for active targeted siRNA delivery, J. Am. Chem. Soc. 137 (48) (2015) 15217–15224.

[25] H.J. Kim, M. Oba, F. Pittella, T. Nomoto, H. Cabral, Y. Matsumoto, K. Miyata, N. Nishiyama, K. Kataoka, PEG-detachable cationic polyaspartamide derivatives bearing stearoyl moieties for systemic siRNA delivery toward subcutaneous BxPC3 pancreatic tumor, J. Drug Target. 20 (1) (2012) 33–42.

[26] S. Matsumoto, R.J. Christie, N. Nishiyama, K. Miyata, A. Ishii, M. Oba, H. Koyama, Y. Yamasaki, K. Kataoka, Environment-responsive block copolymer micelles with a disulfide cross-linked core for enhanced siRNA delivery, Biomacromolecules 10 (1) (2009) 119–127.

[27] T.A. Tockary, K. Osada, Y. Motoda, S. Hiki, Q. Chen, K.M. Takeda, A. Dirisala, S. Osawa, K. Kataoka, Micelles: rod-to-globule transition of pDNA/PEG–Poly(l-Lysine) polyplex micelles induced by a collapsed balance between DNA rigidity and PEG crowdedness (small 9/2016), Small 12 (9) (2016) 1244, 1244.

[28] T.A. Tockary, K. Osada, Q. Chen, K. Machitani, A. Dirisala, S. Uchida, T. Nomoto, K. Toh, Y. Matsumoto, K. Itaka, K. Nitta, K. Nagayama, K. Kataoka, Tethered PEG crowdedness determining shape and blood circulation profile of polyplex micelle gene carriers, Macromolecules 46 (16) (2013) 6585–6592.

[29] K.M. Takeda, K. Osada, T.A. Tockary, A. Dirisala, Q. Chen, K. Kataoka, Poly (ethylene glycol) crowding as critical factor to determine pDNA packaging Scheme into polyplex micelles for enhanced gene expression, Biomacromolecules 18 (1) (2017) 36–43.

[30] A. Dirisala, K. Osada, Q. Chen, T.A. Tockary, K. Machitani, S. Osawa, X. Liu, T. Ishii, K. Miyata, M. Oba, S. Uchida, K. Itaka, K. Kataoka, Optimized rod length of polyplex micelles for maximizing transfection efficiency and their performance in systemic gene therapy against stroma-rich pancreatic tumors, Biomaterials 35 (20) (2014) 5359–5368.

[31] H. Wang, C.A. Thorling, X. Liang, K.R. Bridle, J.E. Grice, Y. Zhu, D.H. Crawford, Z. P. Xu, X. Liu, M.S. Roberts, Diagnostic imaging and therapeutic application of nanoparticles targeting the liver, J. Mater. Chem. B 3 (6) (2015) 939–958.

[32] H. Cabral, Y. Matsumoto, K. Mizuno, Q. Chen, M. Murakami, M. Kimura, Y. Terada, M.R. Kano, K. Miyazono, M. Uesaka, N. Nishiyama, K. Kataoka, Accumulation of sub-100 nm polymeric micelles in poorly permeable tumours depends on size, Nat. Nanotechnol. 6 (12) (2011) 815–823.

[33] L. Nuhn, S. Tomcin, K. Miyata, V. Mailänder, K. Landfester, K. Kataoka, R. Zentel, Size-dependent knockdown potential of siRNA-loaded cationic nanohydrogel particles, Biomacromolecules 15 (11) (2014) 4111–4121.

[34] Y.-N. Zhang, W. Poon, A.J. Tavares, I.D. McGilvray, W.C.W. Chan, Nanoparticle–liver interactions: cellular uptake and hepatobiliary elimination, J. Contr. Release 240 (2016) 332–348.

[35] A.T. Press, A. Traeger, C. Pietsch, A. Mosig, M. Wagner, M.G. Clemens, N. Jbeily, N. Koch, M. Gottschaldt, N. Bézière, V. Ermolayev, V. Ntziachristos, J. Popp, M. M. Kessels, B. Qualmann, U.S. Schubert, M. Bauer, Cell type-specific delivery of short interfering RNAs by dye-functionalised theranostic nanoparticles, Nat. Commun. 5 (1) (2014) 5565.

[36] A.T. Press, A. Ramoji, M. vd Lühe, A.C. Rinkenauer, J. Hoff, M. Butans, C. Rössel, C. Pietsch, U. Neugebauer, F.H. Schacher, M. Bauer, Cargo–carrier interactions significantly contribute to micellar conformation and biodistribution, NPG Asia Mater. 9 (10) (2017) e444, e444.

[37] A.C. Rinkenauer, A.T. Press, M. Raasch, C. Pietsch, S. Schweizer, S. Schwörer, K. L. Rudolph, A. Mosig, M. Bauer, A. Traeger, U.S. Schubert, Comparison of the uptake of methacrylate-based nanoparticles in static and dynamic in vitro systems as well as in vivo, J. Contr. Release 216 (2015) 158–168.

[38] B.K. Wilson, R.K. Prud'homme, Nanoparticle size distribution quantification from transmission electron microscopy (TEM) of ruthenium tetroxide stained polymeric nanoparticles, J. Colloid Interface Sci. 604 (2021) 208–220.

[39] K. Osada, H. Oshima, D. Kobayashi, M. Doi, M. Enoki, Y. Yamasaki, K. Kataoka, Quantized folding of plasmid DNA condensed with block catiomer into characteristic rod structures promoting transgene efficacy, J. Am. Chem. Soc. 132 (35) (2010) 12343–12348.

[40] A.Z. Samuel, S. Umapathy, Energy funneling and macromolecular conformational dynamics: a 2D Raman correlation study of PEG melting, Polym. J. 46 (6) (2014) 330–336.

[41] B. Gong, J.-H. Chen, R. Yajima, Y. Chen, E. Chase, D.M. Chadalavada, B.L. Golden, P.R. Carey, P.C. Bevilacqua, Raman crystallography of RNA, Methods 49 (2) (2009) 101–111.

[42] L. Hao, L. Lin, J. Zhou, pH-Responsive zwitterionic copolymer DHA–PBLG–PCB for targeted drug delivery: a computer simulation study, Langmuir 35 (5) (2019) 1944–1953.

[43] Z. Luo, J. Jiang, pH-sensitive drug loading/releasing in amphiphilic copolymer PAE–PEG: integrating molecular dynamics and dissipative particle dynamics simulations, J. Contr. Release 162 (1) (2012) 185–193.

[44] P.J. Hoogerbrugge, J.M.V.A. Koelman, Simulating microscopic hydrodynamic phenomena with dissipative particle dynamics, Europhys. Lett. 19 (3) (1992) 155–160.

[45] X.N. Xie, S.P. Xu, P.H. Pi, J. Cheng, X.F. Wen, X. Liu, S.N. Wang, Dissipative particle dynamic simulation on the assembly and release of siRNA/polymer/gold nanoparticles based polyplex, AIChE J. 64 (3) (2018) 810–821.

[46] Y. Ruiz-Morales, A. Romero-Martínez, Coarse-grain molecular dynamics simulations to investigate the bulk viscosity and critical micelle concentration of the ionic surfactant sodium dodecyl sulfate (SDS) in aqueous solution, J. Phys. Chem. B 122 (14) (2018) 3931–3943.

[47] G. Weber, R. Wildgruber, Free-flow electrophoresis system for proteomics applications, Methods Mol. Biol. 384 (2008) 703–716.

[48] X. Wang, Y. Xia, microRNA-328 inhibits cervical cancer cell proliferation and tumorigenesis by targeting TCF7L2, Biochem. Biophys. Res. Commun. 475 (2) (2016) 169–175.

[49] C. Zhou, D. Tan, L. Chen, X. Xu, C. Sun, L. Zong, S. Han, Y. Zhang, Effect of miR-212 targeting TCF7L2 on the proliferation and metastasis of cervical cancer, Eur. Rev. Med. Pharmacol. Sci. 21 (2) (2017) 219–226.

[50] J.L. Boyer, Bile formation and secretion, Compr. Physiol. 3 (3) (2013) 1035–1078.

[51] R. Gerst, Z. Cseresnyés, M.T. Figge, JIPipe: visual batch processing for ImageJ, Nat. Methods (2023) doi: 10.1038/s41592-022-01744-4.

[52] I. Muljajew, S. Huschke, A. Ramoji, Z. Cseresnyés, S. Hoeppener, I. Nischang, W. Foo, J. Popp, M.T. Figge, C. Weber, M. Bauer, U.S. Schubert, A.T. Press, Stealth effect of short polyoxazolines in graft copolymers: minor changes of backbone end group determine liver cell-type specificity, ACS Nano 15 (7) (2021) 12298–12313.

[53] Z. Cseresnyes, K. Kraibooj, M.T. Figge, Hessian-based quantitative image analysis of host-pathogen confrontation assays, Cytometry 93 (3) (2018) 346–356.

[54] Z. Cseresnyes, M.I.A. Hassan, H.-M. Dahse, K. Voigt, M.T. Figge, Quantitative impact of cell membrane fluorescence labeling on phagocytosis measurements in confrontation assays, Front. Microbiol. 11 (1193) (2020).

[55] W. Foo, A. Wiede, S. Bierwirth, R. Heintzmann, A.T. Press, W. Hauswald, Automated multicolor mesoscopic imaging for the 3-dimensional reconstruction of fluorescent biomarker distribution in large tissue specimens, Biomed. Opt Express 13 (7) (2022) 3723–3742.

[56] S. Li, H. Chen, H. Liu, L. Liu, Y. Yuan, C. Mao, W. Zhang, X. Zhang, W. Guo, C.-S. Lee, X.-J. Liang, In vivo real-time pharmaceutical evaluations of near-infrared II fluorescent nanomedicine bound polyethylene glycol ligands for tumor photothermal ablation, ACS Nano 14 (10) (2020) 13681–13690.

[57] S.R. Popielarski, S. Hu-Lieskovan, S.W. French, T.J. Triche, M.E. Davis, A nanoparticle-based model delivery system to guide the rational design of gene delivery to the liver. 2. In vitro and in vivo uptake results, Bioconjugate Chem. 16 (5) (2005) 1071–1080.

[58] D. Chen, S. Ganesh, W. Wang, M. Amiji, Protein corona-enabled systemic delivery and targeting of nanoparticles, AAPS J. 22 (4) (2020) 83.

[59] N.J. Hunt, G.P. Lockwood, F.H. Le Couteur, P.A.G. McCourt, N. Singla, S.W. S. Kang, A. Burgess, Z. Kuncic, D.G. Le Couteur, V.C. Cogger, Rapid intestinal uptake and targeted delivery to the liver endothelium using orally administered silver sulfide quantum dots, ACS Nano 14 (2) (2020) 1492–1507.

[60] M. Balwani, E. Sardh, P. Ventura, P.A. Peiró, D.C. Rees, U. Stölzel, D.M. Bissell, H. L. Bonkovsky, J. Windyga, K.E. Anderson, Phase 3 trial of RNAi therapeutic givosiran for acute intermittent porphyria, N. Engl. J. Med. 382 (24) (2020) 2289–2301.

[61] A. Alaarg, M.L. Senders, A. Varela-Moreira, C. Pérez-Medina, Y. Zhao, J. Tang, F. Fay, T. Reiner, Z.A. Fayad, W.E. Hennink, J.M. Metselaar, W.J.M. Mulder, G. Storm, A systematic comparison of clinically viable nanomedicines targeting HMG-CoA reductase in inflammatory atherosclerosis, J. Contr. Release 262 (2017) 47–57.

[62] L. Jiang, P. Berraondo, D. Jericó, L.T. Guey, A. Sampedro, A. Frassetto, K. E. Benenato, K. Burke, E. Santamaría, M. Alegre, Á. Pejenaute, M. Kalariya, W. Butcher, J.-S. Park, X. Zhu, S. Sabnis, E.S. Kumarasinghe, T. Salerno, M. Kenney, C.M. Lukacs, M.A. Ávila, P.G.V. Martini, A. Fontanellas, Systemic messenger RNA as an etiological treatment for acute intermittent porphyria, Nat. Med. 24 (12) (2018) 1899–1909.

[63] X.-J. Du, J.-L. Wang, W.-W. Liu, J.-X. Yang, C.-Y. Sun, R. Sun, H.-J. Li, S. Shen, Y.-L. Luo, X.-D. Ye, Y.-H. Zhu, X.-Z. Yang, J. Wang, Regulating the surface poly (ethylene glycol) density of polymeric nanoparticles and evaluating its role in drug delivery in vivo, Biomaterials 69 (2015) 1–11.

[64] V.C. Cogger, J.N. O'Reilly, A. Warren, D.G. Le Couteur, A standardized method for the analysis of liver sinusoidal endothelial cells and their fenestrations by scanning electron microscopy, JoVE (98) (2015) e52698, e52698.

[65] F. Braet, E. Wisse, Structural and functional aspects of liver sinusoidal endothelial cell fenestrae: a review, Comp. Hepatol. 1 (1) (2002) 1–17.

[66] N. Farkas, P.V. Scaria, M.C. Woodle, J.A. Dagata, Physical-chemical measurement method development for self-assembled, core-shell nanoparticles, Sci. Rep. 9 (1) (2019) 1655.

[67] K. Kunath, A. von Harpe, H. Petersen, D. Fischer, K. Voigt, T. Kissel, U. Bickel, The structure of PEG-modified poly(ethylene imines) influences biodistribution and pharmacokinetics of their complexes with NF-κB decoy in mice, Pharmaceut. Res. 19 (6) (2002) 810–817.

[68] H. Petersen, P.M. Fechner, A.L. Martin, K. Kunath, S. Stolnik, C.J. Roberts, D. Fischer, M.C. Davies, T. Kissel, Polyethylenimine-graft-Poly(ethylene glycol) copolymers: influence of copolymer block structure on DNA complexation and biological activities as gene delivery system, Bioconjugate Chem. 13 (4) (2002) 845–854.

[69] S.M. Lee, N. Bond, C. Callaway, B. Clark, E. Farmer, M. Mallard, S.S. Jang, Dissipative particle dynamics simulation of multicompartment micelle nanoreactor with channel for reactants, RSC Adv. 8 (66) (2018) 37866–37871.

[70] S. Zeng, X. Quan, H. Zhu, D. Sun, Z. Miao, L. Zhang, J. Zhou, Computer simulations on a pH-responsive anticancer drug delivery system using zwitterion-grafted polyamidoamine dendrimer unimolecular micelles, Langmuir 37 (3) (2021) 1225–1234.

[71] R.W. Carthew, E.J. Sontheimer, Origins and Mechanisms of miRNAs and siRNAs, Cell 136 (4) (2009) 642–655.

[72] R.L. Kanasty, K.A. Whitehead, A.J. Vegas, D.G. Anderson, Action and reaction: the biological response to siRNA and its delivery vehicles, Mol. Ther. 20 (3) (2012) 513–524.

[73] J. Wu, T.M. Sun, X.Z. Yang, J. Zhu, X.J. Du, Y.D. Yao, M.H. Xiong, H.X. Wang, Y. C. Wang, J. Wang, Enhanced drug delivery to hepatocellular carcinoma with a galactosylated core-shell polyphosphoester nanogel, Biomater. Sci. 1 (11) (2013) 1143–1150.

[74] M.J. Barthel, K. Babiuch, T. Rudolph, J. Vitz, S. Hoeppener, M. Gottschaldt, M. D. Hager, F.H. Schacher, U.S. Schubert, Bis-hydrophilic and functional triblock terpolymers based on polyethers: synthesis and self-assembly in solution, J. Polym. Sci. Polym. Chem. 50 (14) (2012) 2914–2923.

[75] M. Danaei, M. Dehghankhold, S. Ataei, F. Hasanzadeh Davarani, R. Javanmard, A. Dokhani, S. Khorasani, M. Mozafari, Impact of particle size and polydispersity index on the clinical applications of lipidic nanocarrier systems, Pharmaceutics 10 (2) (2018) 57.

[76] K.J. Livak, T.D. Schmittgen, Analysis of relative gene expression data using real-time quantitative PCR and the 2− ΔΔCT method, Methods 25 (4) (2001) 402–408.

[77] R.C.R. Team, A Language and Environment for Statistical Computing, 2013.

[78] C.G. Ryan, E. Clayton, W.L. Griffin, S.H. Sie, D.R. Cousens, SNIP, a statistics-sensitive background treatment for the quantitative analysis of PIXE spectra in geoscience applications, Nucl. Instrum. Methods Phys. Res. Sect. B Beam Interact. Mater. Atoms 34 (3) (1988) 396–402.

[79] H. Wickham, ggplot2. *Wiley Interdisciplinary Reviews: Comput. Stat.* 3 (2) (2011) 180–185.

[80] V. OriginPro, OriginLab Corporation, 2016. Northampton, MA, USA.

[81] BIOVIA, Dassault Systèmes, Materials Studio, 19.1.0.219, Dassault Systèmes, San Diego, 2020.

[82] R.L.C. Akkermans, N.A. Spenley, S.H. Robertson, Monte Carlo methods in materials Studio, Mol. Simulat. 39 (14–15) (2013) 1153–1164.

[83] Y.Z. Mo, J.C. Xu, Studies on mechanical properties and optimization model of PI/SiO2 nanocomposite based on materials Studio, Adv. Mater. Res. 1049–1050 (2014) 54–57.

[84] H. Sun, Z. Jin, C. Yang, R.L. Akkermans, S.H. Robertson, N.A. Spenley, S. Miller, S. M. Todd, COMPASS II: extended coverage for polymer and drug-like molecule databases, J. Mol. Model. 22 (2) (2016) 47.

[85] Y. Benjamini, Y. Hochberg, Controlling the false discovery rate: a practical and powerful approach to multiple testing, J. Roy. Stat. Soc. B 57 (1) (1995) 289–300.